Space Sci Rev (2012) 170:583–640
DOI 10.1007/s11214-012-9921-1

REMS: The Environmental Sensor Suite for the Mars Science Laboratory Rover

J. Gómez-Elvira · C. Armiens · L. Castañer · M. Domínguez · M. Genzer · F. Gómez · R. Haberle · A.-M. Harri · V. Jiménez · H. Kahanpää · L. Kowalski · A. Lepinette · J. Martín · J. Martínez-Frías · I. McEwan · L. Mora · J. Moreno · S. Navarro · M.A. de Pablo · V. Peinado · A. Peña · J. Polkko · M. Ramos · N.O. Renno · J. Ricart · M. Richardson · J. Rodríguez-Manfredi · J. Romeral · E. Sebastián · J. Serrano · M. de la Torre Juárez · J. Torres · F. Torrero · R. Urquí · L. Vázquez · T. Velasco · J. Verdasca · M.-P. Zorzano · J. Martín-Torres

Received: 9 January 2012 / Accepted: 10 July 2012 / Published online: 4 August 2012

J. Gómez-Elvira (✉) · C. Armiens · F. Gómez · A. Lepinette · J. Martín · J. Martín-Torres · J. Martínez-Frías · L. Mora · S. Navarro · V. Peinado · J. Rodríguez-Manfredi · J. Romeral · E. Sebastián · J. Torres · J. Verdasca · M.-P. Zorzano
Centro de Astrobiología (CSIC-INTA), Carretera de Ajalvir, km. 4, 28850 Torrejón de Ardoz, Madrid, Spain
e-mail: gomezej@cab.inta-csic.es

I. McEwan · M. Richardson
Ashima Research, Pasadena, CA, USA

L. Castañer · M. Domínguez · V. Jiménez · L. Kowalski · J. Ricart
Universidad Politécnica de Cataluña, Barcelona, Spain

M.A. de Pablo · M. Ramos
Universidad de Alcalá de Henares, Alcalá de Henares, Spain

M. de la Torre Juárez
Jet Propulsion Laboratory, Pasadena, CA, USA

J. Moreno · A. Peña · J. Serrano · F. Torrero · T. Velasco
EADS-CRISA, Tres Cantos, Spain

N.O. Renno
Michigan University, Ann Arbor, MI, USA

M. Genzer · A.-M. Harri · H. Kahanpää · J. Polkko
FMI, Helsinki, Finland

R. Haberle
NASA Ames Research Center, Moffet Field, CA, USA

R. Urquí
INSA, Madrid, Spain

L. Vázquez
Universidad Complutence de Madrid, Madrid, Spain

Abstract The Rover Environmental Monitoring Station (REMS) will investigate environmental factors directly tied to current habitability at the Martian surface during the Mars Science Laboratory (MSL) mission. Three major habitability factors are addressed by REMS: the thermal environment, ultraviolet irradiation, and water cycling. The thermal environment is determined by a mixture of processes, chief amongst these being the meteorological. Accordingly, the REMS sensors have been designed to record air and ground temperatures, pressure, relative humidity, wind speed in the horizontal and vertical directions, as well as ultraviolet radiation in different bands. These sensors are distributed over the rover in four places: two booms located on the MSL Remote Sensing Mast, the ultraviolet sensor on the rover deck, and the pressure sensor inside the rover body. Typical daily REMS observations will collect 180 minutes of data from all sensors simultaneously (arranged in 5 minute hourly samples plus 60 additional minutes taken at times to be decided during the course of the mission). REMS will add significantly to the environmental record collected by prior missions through the range of simultaneous observations including water vapor; the ability to take measurements routinely through the night; the intended minimum of one Martian year of observations; and the first measurement of surface UV irradiation. In this paper, we describe the scientific potential of REMS measurements and describe in detail the sensors that constitute REMS and the calibration procedures.

Keywords Mars · Mars Science Laboratory · Atmosphere · Meteorology · Pressure · Relative Humidity · Wind · Ultraviolet radiation · Temperature

1 Introduction

One of the most remarkable characteristics of Mars is that it possesses an atmosphere in many ways similar to that of the Earth, that may have been even more similar in the past. It is the presence of a dynamic atmosphere, and the story of dramatic climate variations that most intrigue us about Mars, including the possibility that a moist climate appropriate to life once may have existed there. Mars continues to have an interesting climate system to this day and its climate may still allow habitable zones near the surface (Jakosky et al. 2005). Currently Mars is known to support aeolian processes—dust lifting and sand transport by winds—that dominate contemporary geological activity (Sullivan et al. 2005). It also has an active water cycle that exchanges water between the subsurface and atmosphere (Jakosky et al. 1997) on seasonal and diurnal timescales, and may move substantial amounts of ground ice over obliquity time scales. Mars' thin atmosphere, lack of oceans, and widespread coating of low thermal inertia dust favor large seasonal and diurnal temperature variations (Tillman et al. 1994; Smith 2008; McCleese et al. 2010). Intense horizontal and vertical winds develop near the surface, which compensate for the low density of the atmosphere and yield widespread dust devil activity and dust storms that grow to global events.

The Martian atmosphere can be divided in 3 vertical regions: an upper atmosphere with very high temperatures and where mixing is weak such that different gases start to have separate scale heights; a middle atmosphere with a strong winter polar jet stream; and, a lower atmosphere dominated by turbulent interactions with the surface and strong mesoscale circulations forced by topography and horizontal temperature contrasts. The Planetary Boundary Layer (PBL) is the dynamically varying region of the lower atmosphere where heat, momentum, water, dust and other tracer species are directly exchanged by turbulent mixing the atmosphere and the surface. On Mars, the PBL varies greatly in depth and properties depending strongly on the local time, but also on location, season, and the atmospheric

dust and water ice opacity. During the day, intense convection may take place, with plumes and vortices rising to heights in excess of 10 km (Haberle et al. 1993a; Larsen et al. 2002; Fisher et al. 2005; Hinson et al. 2008). At night, convection is inhibited and radiative cooling produces a stably stratified layer at the surface, and the PBL reduces to a shallow layer (as little as a few 10's of meters deep) forced by mechanical turbulence at the bottom of the stable layer.

Our understanding of the Martian climate has increased greatly in the last 15 years—a period of nearly continuous orbiter observations. Mars Global Surveyor, Mars Express, the Mars Odyssey, and the Mars Reconnaissance Orbiter have provided new information about the Martian climate, which is characterized by extreme seasonality that results from the high eccentricity of the orbit of Mars. Nevertheless in spite of the great increase in spacecraft observations, the near surface remains one of the least understood regions of the atmosphere. The near surface is not particularly amenable to observations from orbit because the processes of interest generally occur on spatial scales too small to be resolved. In addition, quantitative orbital remote sensing techniques like infrared radiometery have difficulty retrieving information within the lowest few kilometers to scale height of the surface due to the strong surface/atmosphere temperature contrasts. Only the rather sparse and irregular high resolution data from radio occultation observations are of particular use for study of this important region of interchange between the surface and atmosphere (Kliore et al. 1965).

A good understanding of Martian lower atmospheric processes and the ability to simulate them with climate models is necessary for the potential planning of future safe operations of humans at the surface, and is a concern even for robotic mission operations. To compensate for limited data, models based on the relatively well understood circulation and thermal structure of Earth's atmosphere have been developed to study Mars (e.g. Haberle et al. 1993b; Forget et al. 1999; Rafkin et al. 2001; Richardson et al. 2007). As on Earth, numerical modeling of the Martian atmosphere has been applied at a range of scales: from the typically low-resolution (≈300 km) General Circulation Models (GCM) to the higher resolution limited area mesoscale (≈10–100 km) and microscale or Large Eddy Simulation (LES) models. Unfortunately, on the smallest scales and in the crucial region of the surface-atmosphere interface, the models are not well constrained by current data. *In situ* measurements of near surface wind, temperature, moisture, and pressure are necessary to constrain the models and these measurements require a set of dedicated meteorological sensors such as those provided by REMS.

A separate concern for habitability is the ultraviolet (UV) irradiation of the surface and lower atmosphere. UV radiation ionizes atmospheric gases and damages life as we know it. For this reason, knowledge of the UV radiation flux and its spectrum at the surface of Mars is important for the understanding current habitability conditions. Moreover, UV radiation is a significant driver of photochemistry in the atmosphere and on the surface. REMS is the first *in situ* instrument capable of measuring the UV radiation reaching Mars' surface.

Several meteorological stations have predated REMS on the Martian surface, each one with its own characteristics. A comparative list of all the meteorological stations flown to the Mars surface is shown in Table 1. The main distinguishing characteristics of REMS are its ability to measure: vertical winds, the downward ultraviolet radiation at the surface, time series of surface temperature along with simultaneous atmospheric temperatures and winds, and the ability to measure time series of relative humidity within the context of simultaneous meteorological fields and surface temperatures. The simultaneity of multiple, consistent, and constraining environmental variables is essential for meaningful interpretation of near-surface processes.

The goal of REMS is to provide insights into habitability, atmospheric processes and surface/atmosphere interactions from its crucial vantage point at the surface within Gale

Table 1 Comparison between the design science requirements of Mars meteorological stations flown before REMS (Chamberlain et al. 1976; Seiff et al. 1997; Smith et al. 2006; Taylor et al. 2008). In Sect. 4.14 are summarized the REMS performance, which allows comparison with the missions shown in this table

Variable	Vikings V1, V2	Mars Pathfinder	MERs O, S	Phoenix
Temporal coverage	V1 Jul 20 1976–Nov 1982 2245 Sols V2 Sep 3 1976–Apr 1980 1281 sols	Jul 4, 1997 83 Sols	O 25 Jan 2004–current S Jan 4, 2004 +2210 sols	Aug 4, 2012 +152 Sols
Landing location	V1 22.7 °N × 312.05°E V2 47.62 °N × 134.23 °E −2.69 km/4.23 km altitude	19.09 °N × 326.74 °E −2.8 km	O 1.95 °S × 175.47 °E S 14.57 °S × 354.47 °E	68.21 °N × 234.25.4 °E −4.45 km
Wind	Two hot film sensors, placed 90 deg apart horizontally. Overheated 100 °C above ambient Accuracy 10 % for wind speed <2 m/s Horizontal Wind direction Quadrant sensor: a heated center post with four thermocouples around it. Accuracy 10 % Sampling <0.8 Hz	Hot wire sensor about 1.3 m above surface. Wind speed Accuracy: 1 m/s for wind speed <20 m/s 4m/s for wind speed >20 m/s Wind direction resolution: 10° Sampling 0.25 Hz & 1 Hz	N/A	No regular time series measurements, only occasional imaging of a weather vane: Range: 1 m/s–5 m/s Accuracy: 1 m/s Range: 5 m/s–10 m/s Accuracy: 20 % (40 % along the SSI camera line of sight) Sampling: semidiurnal
Pressure	Inside the Lander body Accuracy 9 Pa	Inside the Lander body Accuracy <1 Pa	N/A	0–5 hPa ±10 % occasional with TEGA Sampling rate: 0.1 Hz
Boundary layer structure	N/A	N/A	Thermal profiling with mini-TES	LIDAR for aerosol profiling.
Soil surface temperature	N/A	N/A	Surface thermal spectra from mini-TES	8 Sols of contact measurements with Thermal and Electrical Conductivity Probe (TECP) on MECA Sampling: each 15 min
Near surface air humidity	N/A	N/A	N/A	N/A
Near surface air temperature	Three parallel-wired chromed-constantan thermocouples at the end of a boom, 1.6 m above ground, 0.3 m away from Lander body horizontally (to avoid thermal contamination from the Lander body)	Thermocouples at three altitudes from surface: 1.27 m, 0.77 m. 0.52 m Accuracy ±1 K	0–1 m average and profile to 5 km with mini-TES Sampling: Typically one profile mid-morning and one mid-afternoon	At three heights 0.5 m, 1 m, 1.5 m Sampling rate: 0.5 Hz Range 140 K–280 K Absolute accuracy: ±1 K Resolution: 0.5 K

Fig. 1 Gale Crater and MSL landing ellipse. (Credits: NASA/JPL/University of Arizona)

Crater. REMS is intended to operate for 2 Earth years, during which time it will acquire data every hour, for 5 minutes each and at a sampling rate of 1 Hz, on the wind speed and direction, air and ground temperature, atmospheric humidity, pressure and UV irradiation. These measurements will enable analysis of diurnal and seasonal environmental variations and provide the first measurements of UV radiation incident on the Martian surface. It should also be noted that the regularity of planned higher observation sampling frequencies (1 Hz) and the expected observation period should bring REMS closer to the extended baseline provided by Viking than any meteorological instrument in the last 30 years.

MSL will land and operate within Gale Crater (see Fig. 1). Gale provides a far more complex meteorological environment than that sampled by prior missions due to the large and varied topography. The crater is 154 km in diameter and is located in the north-eastern portion of the Aeolis quadrangle on the boundary between the southern cratered highlands and the lowlands of Elysium Planitia. Both its location and morphology make Gale an interesting place from a meteorological point of view. Sitting just south of the equator (4.6 °S 137.2 °E), Gale Crater is expected to be situated in the seasonally reversing 'trade wind' or 'monsoon' circulation of the surface branch of the tropical overturning circulation (sometimes—possibly inaccurately—referred to as the 'Hadley circulation'). Gale also sits on the edge of the dichotomy boundary, which tends to be associated with somewhat intensified day/night circulation. The complexity of the expected meteorological context doesn't stop there since Gale Crater is characterized by a massive elevation change between the expected landing site, sitting about 4 km below datum, and the layered Mt. Sharp near the crater center, which reaches up to almost 1.5 km above datum. This mountain in the center of the crater may result in significant local day/night slope winds. The orientation and distribution of dark surfaces around the peak and extending to the south of the crater also suggests that wind scouring of dust is an active process, at least during some seasons (most likely southern summer). Being close to the equator, thermal tide signatures at Gale should be strong and may yield information on the global scale dust heating of the atmosphere and the large scale distribution of winds. The signature of far reaching mid latitude baroclinic systems may also be detectable.

2 Science Objectives

The REMS measurements will provide useful information for studies of atmosphere processes ranging from local to synoptic scales. In particular REMS will provide data for studies of the following processes:

– Microscale dynamics;
– Mesoscale dynamics;
– Synoptic meteorology and dust storms;
– The local UV radiation environment;
– The local water vapor and dust cycles.

The REMS data will be useful for studies of microscale dynamics focusing on boundary layer processes such as atmospheric convection and the dynamics of the nocturnal boundary layer, for studies of mesoscale dynamics focusing on the effects of topography and surface properties such as thermal inertia and albedo on microscale and mesoscale dynamics (Petrosyan et al. 2011). A combination of REMS measurements with that from other MSL instruments will be useful for studies of the cycles of dust and volatiles such as water vapor, while a combination of REMS measurements with that from orbiters will be useful for studies of the effects of synoptic scale processes on the local meteorology and the UV radiation environment.

2.1 Microscale Dynamics: Characterization of the Near Surface Meteorological Environment

REMS will characterize the near-surface meteorological environment by measuring air temperature, ground temperature, atmospheric pressure, humidity, wind, and UV radiation. The Martian surface experiences much greater variations in temperature than that of the terrestrial surface (Petrosyan et al. 2011). This forces more intense atmospheric convection and deeper PBL during the day, as well as stronger near-surface temperature inversion during the night. These large variations in the properties of the PBL have a major impact on the exchange of heat, momentum, dust, and water between the surface and the atmosphere (Petrosyan et al. 2011). REMS will shed new light on these processes by making hourly measurements at high sampling rate for at least one Mars year.

2.1.1 Turbulence

Measurements of temperature and wind at 10–100 Hz are necessary to properly characterize turbulence in the Martian atmosphere (Petrosyan et al. 2011). Unfortunately continuous measurements at high sampling rates are not possible yet from a Mars lander because of large constraints on mass, power and data volume. Instead, turbulence can be studied using a combination of measurements at lower sampling rate and theory (Tillman et al. 1994). This is the approach taken by REMS, on which hourly measurements made a sampling rates of up to 1 Hz are used in combination with theory to study microscale atmospheric phenomena. A combination of measurements of temperature and wind at up to 1 Hz with data from Large Eddy Simulation (LES) numerical models will then be used to study turbulent motions. REMS measurements at 1 Hz for at least 5 minutes at each hour will provide insights into near-surface turbulence and their role on atmospheric-surface interaction.

Dry Convective Vortices or "Dust Devils" REMS will sample dry convective vortices such as dust devils and will study their role in the local dust cycle. Dust devils have been sampled by the Viking and Mars Pathfinder landers and have been imaged from the surface by the Mars Pathfinder, the Phoenix Lander, and the Mars Exploration Rovers (Renno et al. 2000; Ferri et al. 2003; Holstein-Rathlou et al. 2010; Greeley et al. 2010). Modeling and analysis of the images of the Mars Pathfinder indicate that dust devils play an important role in the Martian dust cycle (Ferri et al. 2003). While global dust storms are the most dramatic aspect of the Martian dust cycle, the fluxes of heat and momentum are quantities that determine the exchanges of dust, water, energy and momentum between the surface and the atmosphere. The permanent atmospheric haze that is maintained by dust devils appears to have greater climatological importance than the large-scale dust storms (Ferri et al. 2003); without the ubiquitous dust haze, the mean mid-level (10 to 40 km) air temperatures would be roughly 5–10 K cooler throughout the year. REMS will study dust devils in a region of dramatic topography that has not been studied before. Since convective circulations are expected to be intense in this region, it might shed new light on the role of dust devils in the Martian dust cycle. REMS identifies dust devils as sharp pressure drops (of a few Pa or $\sim$1 %) associated with increases in temperature and a rapid rotation of the winds. By making hourly measurements at 1 Hz for a Mars year, REMS is expected to characterize dust devils better than previous Mars missions. REMS will also characterize other convective structures such as convective cells and gust fronts. LES and high-resolution mesoscale simulations predict that bands of relatively low and high pressure perturbations associated with up- and down-drafts within convective cells are common on Mars (Petrosyan et al. 2011), REMS is expected to detect these atmospheric structures in situ for the first time. Measurements of these atmospheric structures would provide strong constraints on theory and modeling of the Martian PBL, and shed light on their scales and velocities.

2.2 Mesoscale Dynamics

Most of what is known about mesoscale weather systems on Mars is based on theory and numerical modeling. Mesoscale flows include a disparate range of dynamical structures grouped together on the basis of scale. The mesoscale typically includes (is defined as) motions larger than those that occur within PBL turbulence but smaller than the synoptic scale motions of the tropical overturning circulation, large-scale atmospheric waves, and mid-latitude low pressure cyclones. The dynamics of frontal evolution within such cyclones is within the mesoscale purview, however. Of more relevance to MSL in the tropical Gale Crater are mesoscale motions driven by sharp topographic and thermal contrasts. REMS will provide unique data on mesoscale circulations because of the range of measurements it collects with good diurnal sampling; because MSL will land in a location expected to generate a range of mesoscale systems; and, because as a rover-based system, REMS will be able to sample a large number of different sites within the Gale Crater system.

Numerical models suggest that variations in surface properties and topography will force diurnally-reversing flows, such as flows up-and-down the extended walls of the crater and the central Mt. Sharp. The strength of such flows in relationship to the topography and known thermal forcing will help to constrain mesoscale models of these flows. Differential heating associated with these contrasts are expected to generate migrating air masses with associated mesoscale fronts (also know as 'microfronts' to distinguish them from fronts associated with mid-latitude low pressure cyclones that are unlikely to be seen at Gale Crater). These fronts would appear in REMS data as sharp temperature changes, associated with changes in wind speed and direction. Fronts are frequently created as cold air drains off a crater rim or mesa

plateau and flows across a plain. The cold air undercuts warmer environmental air, pushing it up and out of its way. Sharp fronts can develop if the onset of air flow is abrupt, with cold microfronts expected to be narrower and more conspicuous than warm fronts, and thus easier to identify in REMS data. REMS observations of microfronts may also be of use in quantifying their role in dust lifting and local dust storm origination if there is evidence of active eolian transport of dust from simultaneous camera imaging.

2.3 Synoptic Dynamics

Long time-series of *in situ* measurements will provide unique information about the global atmosphere. Four Landers thus far have acquired such observations (Viking Landers 1 and 2, Mars Pathfinder, and Phoenix), but none with the regularity and continuity planned by the REMS investigation. Thus, MSL will provide a unique meteorological data set for the scientific community. Acquisition of these data in concert with thermal sounding from the Mars Climate Sounder and imaging from the Mars Color Imager, both aboard Mars Reconnaissance Orbiter (MRO), will yield unprecedented insight into the global atmospheric circulation. Three major types of large-scale systems can potentially be studied with REMS: thermal tides, mean large-scale circulations, and low-pressure weather systems. The thermal tides are in many ways the most diagnostically useful.

Thermal tides are global-scale wave systems excited by the diurnal cycle of solar forcing. Because the forcing function is not a smooth sine wave (the forcing is zero throughout the night) and because of complex interactions with topography and other waves, harmonics at frequencies above the diurnal are present. These tides are evident in pressure and wind data, but more evident in the former. The tidal response of the atmosphere varies with the harmonic, but is sensitive to the global wind distribution and atmospheric dust abundance, through the influence of dust on atmospheric radiative heating. Indeed, it has been shown that the amplitude of semidiurnal tides provides a useful constraint on the total atmospheric dust opacity. Should large dust storms occur at locations hundreds or thousands of kilometers from the MSL rover, REMS pressure data will thus still provide uniquely valuable data on the response of the atmosphere and that will help constrain global climate models. Large-scale dust storms did not occur during the Pathfinder mission, and therefore only the Viking surface pressure records have been available for study of their effect on thermal tides. Nonetheless, the existence of these data make the Viking dust storm observations in many ways more valuable than the otherwise better observed 2001 global dust storm. REMS will fill this gap in the event of a dust storm during MSL operations.

2.4 Local UV Radiation Environment and Surface Habitability

The ultraviolet (UV) irradiance sensor will provide in-situ measurements of the UV radiation on the Martian surface during at least two years of nominal mission length. Several science goals shall be achieved by analysis of the measured irradiance.

Atmospheric Constituents: Dust and Ozone Solar UV irradiance is absorbed and scattered by gases and dust particles in the Martian atmosphere (Zorzano and Córdoba-Jabonero 2007). While CO_2 absorbs most of the radiation at wavelengths shorter than 200 nm, at longer wavelengths, the strong terrestrial ozone absorption is not present due to the presence of O_3 in only trace amounts. Also unlike for the Earth, dust aerosols provide significant opacity. Thus the Martian UV radiative transfer scenario is very different from that of the Earth, where molecular ozone absorption and Rayleigh scattering by the dense atmosphere are both more significant than the aerosol extinction. A further complexity is that

the aerosol sizes are comparable to the UV wavelengths, and thus scattering is more complex than molecular Rayleigh scattering (if the particles are approximated as spheres, Mie scattering theory can be used).

REMS observations will allow the direct and diffuse UV irradiance to be determined as the Sun moves across the sky within and outside of the instrument field of view and by using the rover mast to block the direct beam. Using the direct irradiance measurements in the different bands observed by REMS, spectral opacities can be calculated given the known downwelling solar UV. These opacities provide information on the aerosol abundances and particle size distribution, the scattering/absorbing properties of the aerosols, and the abundance of ozone (Zorzano and Córdoba-Jabonero 2007; Zorzano et al. 2009). The ozone concentration may in turn be used as a proxy for atmospheric water vapor, since their presence is anti-correlated.

Validation for Radiative Transfer and Retrieval Models Previous studies of the Martian UV environment have focused on remote observations. Remote sensing in the UV has been undertaken by Mariner 7 and 9 (Barth and Hord 1971; Barth et al. 1973), Phobos-2 in the UVA region (Moroz et al. 1993), the Hubble Space Telescope (James et al. 1994), and most recently by SPICAM (Perrier et al. 2006) and MARCI (Wolff et al. 2010). Radiative transfer codes, that can cope with Mie multiple scattering and arbitrary observation geometries, must be used to retrieve an estimate of the surface UV flux or the total column of ozone from orbiter based observations. These models make certain assumptions about the values of unknown critical parameters of the scattering and reflection processes such as the surface UV reflectance (UV albedo) properties, vertical dust profile, dust absorption and scattering parameters, etc. The REMS-UV sensor will measure, for the first time, at least two years of continuous, and systematic, surface based UV direct and diffuse spectral irradiance measurements and will provide ground-truth to the orbiter based measurements and allow for better tuning of key parameters of the radiative transfer models.

Surface Habitability and Chemistry UV photons have enough energy to excite and remove electrons from atoms and molecules, inducing the formation of radicals and ions. Some of these products may recombine in a chemical reaction leading to the formation of new molecules. A reliable knowledge of the UV radiation levels on the Martian surface is thus important for photochemical models of the atmosphere (Rodrigo et al. 1990), for the chemistry of the surface minerals and the formation of oxidating radicals (Mukhin et al. 1996; Yen et al. 2000; Quin et al. 2001) and, because of its interaction with organic molecules, is paramount for the estimate of biological doses (Cockell et al. 2000; Patel et al. 2002, 2003, 2004a, 2004b; Cordoba-Jabonero et al. 2003, 2005). In particular, the most relevant organic molecules, nucleic acids (DNA and RNA) and proteins, which are furthermore common to all known living forms, are very sensitive to UV radiation. Nucleic acids show a strong absorption band in the range of 260 nm and proteins in the range of 280 nm. Therefore a high level of UV radiation can totally dissociate these molecules and sterilize a surface. The adverse Mars surface conditions are restrictive for life as we know it on Earth but a very thin regolith layer or snow cover can play a protective role for making the conditions compatible for microbial life as it was reported by Amaral et al. (2007), Gómez et al. (2010) and Cordoba-Jabonero et al. (2005). The simultaneous measurements provided by RAD, the particle detector instrument of the MSL rover, and REMS-UV sensor will help understanding the radiation environment on Mars and its implication on surface sterilization processes and dissociation of organic molecules.

2.5 Volatile and Dust Cycles

There are three fundamental climate cycles that need to be understood if we are to gain predictive understanding of the Martian atmosphere and climate. These are the cycles of the two dominant volatiles, CO_2 and water, and that of dust. Based on existing data and heavily leaning on numerical models, we believe we understand the basic outline of these cycles. However, we need more data, especially at the surface, to test our theories of surface/atmosphere exchange and to determine the roles of reservoirs such as the regolith for the water cycle. In most cases, many aspects of the processes are not well understood.

The Seasonal CO_2 Cycle Viking observations suggest that the dominant seasonal surface pressure variations are due to the cycling of the seasonal CO_2 polar ice caps. This suggestion is in good agreement with model predictions and other spacecraft observations and is widely accepted. Open questions exist in regard to why the seasonal cycles observed by Viking were so repeatable despite differences in dust activity and if the cycle is in long-term balance. REMS measurements will provide additional constraints for models of the CO_2 cycle by providing a long-term time series of pressure data at a tropical site where the dynamical contribution to surface pressure is expected to be relatively small. REMS pressure measurements may also be able to determine if the south polar residual cap is disappearing as hypothesized based on images of the southern residual polar cap. The purported rate of disappearance is estimated to be equivalent to an increase in global mean pressures of about 1 % of the present atmospheric mass per Mars decade (Malin et al. 2001). By the time MSL begins surface operations, the expected rise in global mean surface pressures since Viking is $\sim$15 Pa (see Haberle and Kahre 2010 for details), which should be detectable in REMS pressure data provided, there is no significant post-launch change in the calibration of its pressure sensors.

The Water Cycle Martian atmospheric water vapor observations require water to be exchanged between the surface/subsurface and atmosphere on seasonal timescales. Exchange almost certainly occurs with the seasonal and residual polar water ice caps, and may also involve the adsorption/desorption of water from the regolith. However, the relative importance of these processes is not well constrained. The dynamics of water transport depends on the interplay of surface characteristics (soil water content, porosity, albedo, composition, and stratigraphy), atmospheric conditions (stability, circulation patterns) and insolation (variable on diurnal, seasonal and geological time scales).

The Martian PBL plays an important role in the exchange of water between the surface and the free atmosphere (Jakosky et al. 1997). The sublimation/desorption of water from the regolith is regulated by both turbulent and molecular processes. REMS vapor measurements along with the PBL measurements mentioned in Sect. 2.1 will provide insight into how and to what degree water exchanges between the atmosphere and the local surface/subsurface and help constrain the role of the regolith in the water cycle. These measurements, in combination with ground temperature and surface compositional information may also allow insight into the thickness of the soil active layer on Mars and its freezing/sublimation water dynamics (Ramos et al. 2012).

The Dust Cycle Suspended dust is a major modulator of the atmosphere and climate of Mars because of its impact on radiative heating of the surface and atmosphere. REMS will provide a global monitoring of atmospheric dust via the thermotidal signature in the surface pressure observations (see Sect. 2.3). These observations will not only allow the seasonal

Table 2 Relationship between the REMS science objectives, sub-objectives, required measurements, and the required measurement sampling rates and intervals.

Objective	Sub-objectives	Required measurements	Sampling	Regularity
Meteorology	PBL, dust devils, and turbulence	Pressure, ground and air temperature, 3D wind	1 Hz or better	Hourly or better
	Mesoscale systems	Pressure, temperature, wind	1 Hz	Hourly or better
	Large-scale circulation and tides	Pressure, temperature, wind	0.1–0.01 Hz	Hourly
UV irradiation	Dust and ozone abundance	UV radiation	0.1–0.01 Hz	Hourly during daylight
	Surface habitability and photochemistry	UV radiation, air and ground temperature, humidity	0.1–0.01 Hz	Hourly during daylight
Water, CO_2 and dust cycles	CO_2 cycle	Pressure	0.1–0.01 Hz	Hourly if possible
	Water cycle	Pressure, ground and air temperature, wind and humidity	0.1 Hz or better	Hourly or better
	Dust cycle	Pressure, temperature, UV, wind	0.1 Hz or better	Hourly or better

evolution of dust to be assessed, but will also provide crucial information should a large dust storm develop during the MSL mission. REMS will also provide information on conditions necessary for dust lifting, should aeolian transport of dust be observed at Gale by the MSL or orbiter cameras.

3 REMS Design Requirements

The overaching goal of REMS is to assess the current habitability at the Martian surface at the MSL landing site. Habitability is determined on the basis of: environmental conditions, which are in turn determined by meteorology; solar irradiance and especially the UV irradiance at the surface; and, by the cycling of water. The investigation goal consequently maps to objectives of understanding meteorology on various scales, the UV irradiance, and volatile cycles (Table 2). The objectives in turn dictate a specific set of measurements. Meteorology requires the thermal state, air motions, and pressure to be measured; UV irradiance requires direct measurement; and, the cycling of water requires measurement of humidity in addition to those measurements required for meteorology. Specific requirements on these measurements[1] are as further discussed in this section and as summarized in Table 2.

– Air and ground temperature. The diurnal variation of air temperature will be not less than 10 K in dusty conditions and not more than 100 K under clear skies. The accuracy levels of air temperatures must at least allow diurnal cycle monitoring under even the dustiest of conditions. Ground temperature variation requirements are similar.

[1] REMS requirements were established on 2004, at the beginning of the project. Actual performances are summarized in Sect. 4.14.

  - The REMS shall be able to measure ground brightness temperature over the range of 150 to 300 K with a resolution of 2 K and an accuracy of 10 K.
  - The REMS shall be able to measure the temperature of air near the booms over the range of 150 to 300 K with a resolution of 0.1 K and an accuracy of 5 K.
- Pressure variations are modulated by weather phenomena ranging from small to large-scales. The requirements have been set to distinguish global normal modes with periods of 1.1 sol from the diurnal tides or to detect fronts associated with pressure changes as low as 0.1 mbar. The accuracy has been established based on the amplitudes of the general circulation components or dust devils oscillations.
  - The REMS shall be able to measure ambient pressure over the range of 1 to 1150 Pa with a resolution of 0.5 Pa and an accuracy of 10 Pa (beginning of life) and 20 Pa (end of life).
- The atmospheric water vapor abundance is the basic visible manifestation of the seasonal water cycle on Mars. Requirements are defined to be compatible with pressure and temperature requirements.
  - The REMS shall be able to measure ambient relative humidity in the range of 0 to 100 % with a resolution of 1 % and an accuracy of 10 %.
- The radiation measurements range from seasonal to diurnal timescales in the area covered by the MSL rover, plus two channels: Hartley and Huggins bands; to compare with MRO measurements.
  - The REMS shall be able to measure UV radiation in the following 6 bands (with the maximum measurable irradiance in W/m^2):
    Total dose: 210–360 nm (44.7 W/m^2); UVC: 215–277 nm (1.57 W/m^2); UVB: 270–320 nm (6.4 W/m^2); UVA: 315–370 nm (25 W/m^2); UVD: 230–298 nm (5 W/m^2); UVE: 311–343 nm (7.65 W/m^2); with a resolution better than 0.5 % of the maximum measurable irradiance and an accuracy better than 5 % of the maximum measurable irradiance.
  - The REMS UV sensor shall measure UV radiation coming from a solid angle cone of 60 degrees.
- Wind variations reflect the local components of the circulation. This will provide information about surface-layer turbulence and mean vertical gradients, as well as the presence of convective plumes and vortices.
  - The REMS shall be able to measure horizontal wind in the range of 0 to 70 m/s with a resolution of 0.5 m/s and an accuracy of 1 m/s.
  - The REMS shall be able to measure the direction of horizontal wind with a resolution and accuracy better than 30 degrees.
  - The REMS shall be able to measure vertical wind in the range of 0 to 20 m/s with a resolution of 0.5 m/s and an accuracy of 1 m/s.

Regarding the REMS operation the requirements were established as follow:

- The REMS shall be able to operate without interaction with rover avionics
- The REMS shall be capable of collecting and storing sensor data at a sampling rate of 1 Hz, 5 minutes each hour.
- Whenever it detects unexpected changes in meteorological conditions, REMS shall be able to extend its measuring window for an extra period of at least 5 minutes and up to a daily maximum duration to be determined by science planning operations based upon power consumption constraints.

The environmental and operational requirements more significative for the design were:

– The instrument should survive to 1005 cycles from −130° to 15° and 1005 cycles from −105° to 40°. As each cycle represent a day, superimpose to these REMS should add the 5 minutes operation each hour.
– The mission duration should 670 sols.
– A bake out for sterilization purpose of 50 hours at 110° for all elements but the ICU.

4 Instrument Description

4.1 Overview

REMS is composed of four units (see block diagram in Fig. 3): Boom 1, Boom 2, Ultraviolet Sensor (UVS) and Instrument Control Unit (ICU). Boom 1 accommodates a Wind Sensor (WS), an Air Temperature Sensor (ATS) and the Ground Temperature Sensor (GTS), while Boom 2 accommodates a Humidity Sensor (HS) along with a second Wind Sensor and Air temperature Sensor. Both booms include their associated Application-Specific Integrated Circuit (ASIC)-based Sensor Front-End (SFE) electronics. The ICU includes the instrument electronics and the Pressure sensor (PS). The booms are located on the MSL Remote Sensor Mast (RSM) (see Fig. 2), while the UV Sensor is on the rover deck and the ICU-Pressure Sensor package is placed inside the rover body.

Design of scientific instrumentation is always driven by its scientific goals and constrained by engineering and environmental requirements. In particular, to best achieve the REMS science goals, a boom or arm of sufficient length to isolate the sensors from the rover thermal and aerodynamic perturbations would have been required. However, because of imposed engineering requirements (e.g. the REMS boom could not be an obstacle during mast deployment), it was not possible to satisfy this instrument requirement.

The REMS final design thus represents a balance between science goals and vehicle constraints, with the following results: (i) while strictly being too short, the boom length was the maximum allowed by RSM deployment constraints; (ii) two booms were implemented with an angular offset of 120 degrees, so that at least one of them will always be outside of the RSM wake, and (iii) the booms are high enough with respect to the rover deck to minimize the rover body perturbations (430 and 380 mm above rover deck and approximately 1.6 m above the surface). In order to analyze the impact of these engineering constraints, Computational Fluid Dynamics (CFD) simulations with the final rover configuration have been performed.

The components of the REMS instrument are:

1. The Wind Sensors (WS) that are based on hot film anemometry and are composed of three recording points around each Boom. An algorithm combining the data from all the 6 recording points will determine the true wind speed and direction (see Sect. 4.8 for details).
2. The Ground Temperature Sensor (GTS) that records the infrared (IR) brightness temperature of the Martian surface using three thermopiles. The GTS is mounted on Boom 1, and it is directly connected to the Sensor Front-End electronics. The thermopiles look downwards, pointing at the ground alongside the rover and covering an area of about 100 m^2. The sensor includes an active self-calibration system to compensate potential degradation during the mission associated with dust collection on the sensor window (see Sect. 4.2).

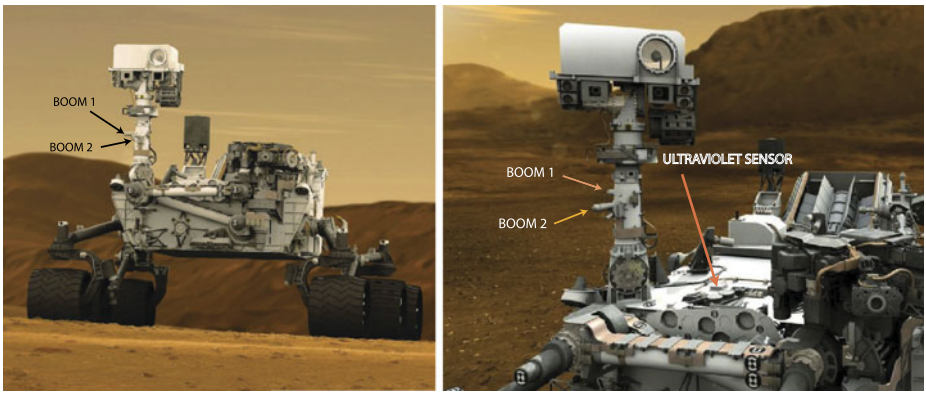

Fig. 2 Artistic view of Curiosity, where the position of the REMS Booms and the Ultraviolet Sensor can be seen. (Credit: NASA/JPL-Caltech)

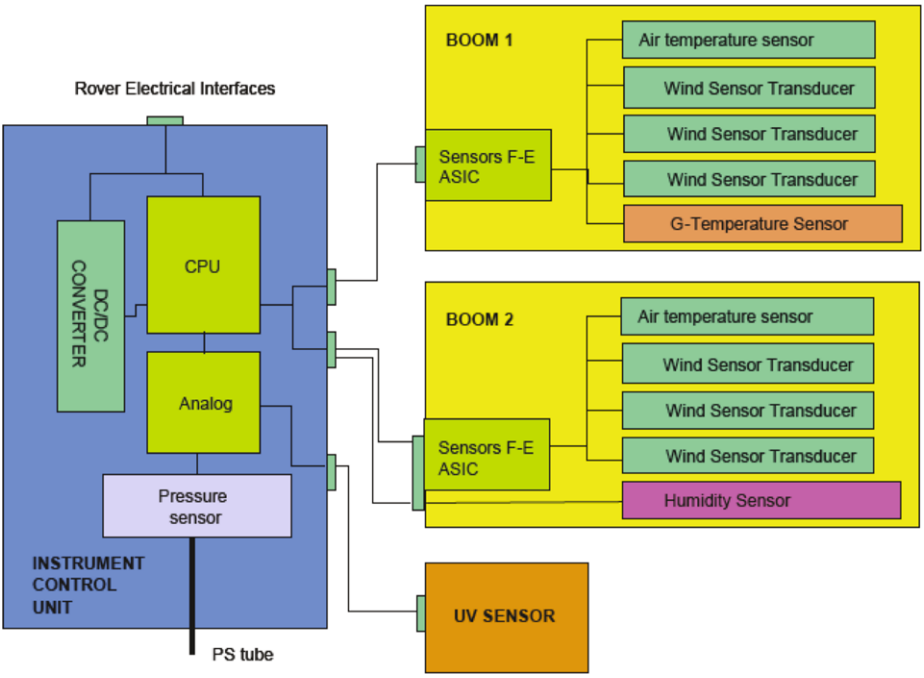

Fig. 3 REMS block diagram. Two booms with a similar mechanical structure; three sensors and a Front-End ASIC for signal conditioning. In Boom 1, the ASIC electronics is in charge of closing wind sensor control loop and processing (amplification and analog-digital conversion) the GTS signals. In Boom 2, the ASIC is only in charge of the WS, since the HS is connected directly to the ICU. Communication ASIC-ICU are digitals to minimize external noise effects. UVS sensor signal is transmitted directly to the ICU

3. The Ultraviolet Sensor (UVS) that is located on the rover deck, and is composed of seven photodiodes (see Sect. 4.10) and a thermistor to monitor the temperature of the UVS. Due to its location, the sensor is exposed to dust deposition and design constraints ruled out

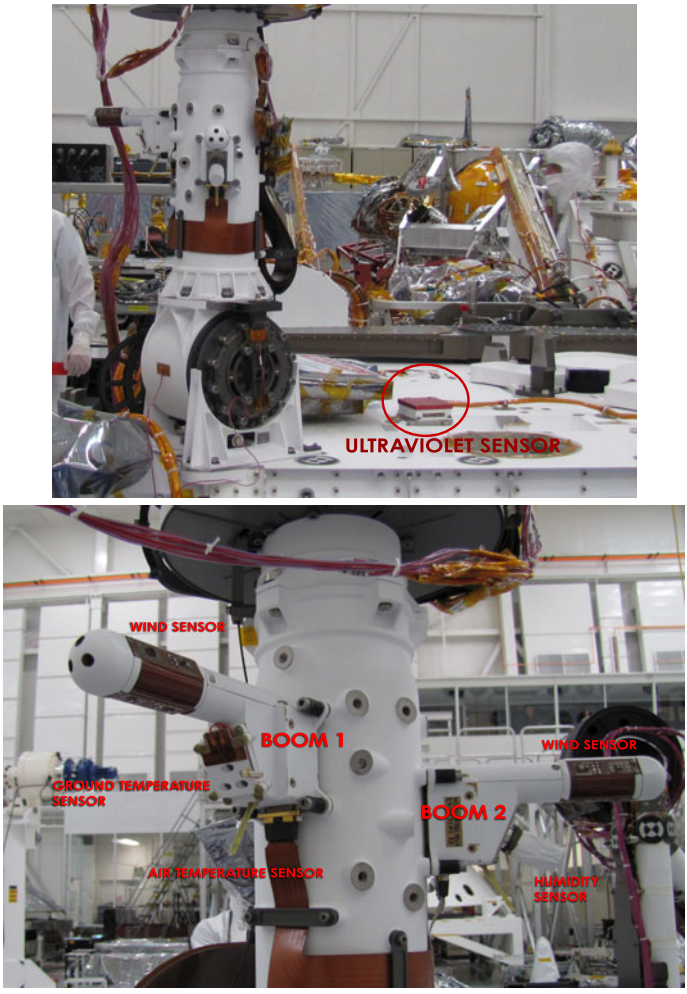

Fig. 4 Images taken during the REMS integration show the position of the REMS sensors. *Top image* shows the location of Booms 1 and 2 and UVS. *Bottom image* is a close-up of both booms. (Credit: NASA/JPL)

any active protection system. Nevertheless, to mitigate the dust degradation effect, each photodiode has a magnet around it, creating a magnetic field that deflects magnetic dust.

4. The Pressure Sensor (PS) that is located in the rover body, and is composed of a Vaisala Barocap® and associated Vaisala Thermocap®, both provided by the Finnish Meteorological Institute (FMI). The FMI pressure sensors have a significant flight heritage, having been flown to Mars on every static lander since Viking.
5. The Humidity Sensor (HS) that is located on Boom 2. The HS is also provided by FMI and is composed of a Vaisala Humicap® relative humidity sensor head and associated Vaisala Thermocap®. The HS, like the PS, is controlled with its own dedicated ASIC, which is in turn controlled and read by a dedicated field programmable gate array (FPGA) inside the REMS ICU.
6. The Air Temperature Sensors (ATS) that are mounted on both booms. They are attached to the lower edge of the SFE ASIC housing, protruding in the direction of the boom

Table 3 REMS dimensions and mass components

Component	Dimensions L × W × H (mm^3)	Mass (kg)
Boom 1	151.27 × 56.18 × 92.4	0.154
Boom 2	151.08 × 56.16 × 93.77	0.147
UVS	55.21 × 68.18 × 19.04	0.89
ICU	120.09 × 120.0 × 79.68	0.853

front-end and under the booms shaft. The sensors are small rods manufactured with low thermal conductivity material and with a thermistor at the tip to measure the ambient temperature. The rod is heated by the boom itself and contaminates the tip thermistor data. To estimate the error induced by this effect, an additional thermistor has been located in the middle of the rod (see Sect. 4.3).

7. The Instrument Control Unit (ICU) (see Sect. 4.13) that provides the interface with the rover in terms of data, telemetry and power, receives digital data from the booms sensors, powers the SFE electronics, and processes data from the PS, HS and UVS. The SFE (Sensor Front-End) ASIC (see Sect. 4.12) in turn provides the sensor electronic interface for the ATS, WS and GTS at boom level. The UVS-ICU communication is analog in order to avoid any electronics at the sensor unit; the harness have been properly shielded to minimize line noise.

An important effect to take into account is the fact that the rover radioisotope thermoelectric generator (RTG) is a constant source of heat, which heats the rover itself but also the fluid around it and the ground illuminated by its infrared radiation. These latter two effects have an impact on the REMS measurements. If the REMS booms happen to be in the lee of the RTG the thermal wake will perturb the air temperature measurements and the steady heat of the RTG may create a standing thermal plume over the rover in low wind situations. More generally, the RTG infrared emission will heat the ground sampled by the GTS.

The REMS design had to abide by stringent restrictions with respect to mass, power and dimensions. Table 3 gives the actual dimensions and mass distribution by components, yielding a total mass of 1.243 kg.

Power consumption will depend on the REMS activity and the ambient temperature. As the booms are not placed in a warm bay, their electronics should be heated to reach their operational temperature. Each Boom ASIC has a heater bound to it, which is switched on when the temperature of the electronics as measured by a dedicated resistance temperature detector (RTD) drops below $-70°$. The REMS power consumption in its different operational modes is as given below:

- Stand by: 402 mW.
- Start-up idle: 4620 mW.
- ASIC heating: 8744 mW.
- All sensors measuring (without ASIC heating): 5432 mW.
- All sensors measuring (with ASIC heating): 10082 mW.
- Data download: 4760 mW.
- Humidity regeneration: 5479 mW.
- GTS calibration: 5174 mW.

4.2 Ground Temperature Sensor

The ground temperature is an important measurement for determination of surface physical properties, for understanding surface/atmosphere exchange and the energetic drive for turbulence, for the energy balance at the surface, and for understanding the stability of water in or in the surface in various phases. The observational requirements are for ground temperature to be measured over the full range expected in the Martian tropics and over the full year (roughly 150–300 K) and with a resolution of 2 K and an absolute accuracy of better than 10 K. Spacecraft resources combined with the need to measure routinely along with the other REMS sensors dictated that deployable contact probes were not practical (indeed, other issues such as determination of the depth of a contact probe measurement combined with the rapid change of temperature within centimeters of the surface present other issues for contact measurements). As such, and based on the precedent set by the MER mini-TES instrument, infrared radiometry was selected for the GTS.

The GTS is located in the REMS Boom 1 positioned on the MSL RSM mast (Fig. 4). The sensor is based on broad-band IR thermopile sensors and uses three filters to sample the ground longward and shortward of the 15-micron CO_2 absorption feature and also centered on that feature. The GTS also hosts the electronics employed to amplify thermopile signals.

To avoid small-scale temperature effects brought about, for instance, by shadowing by individual rocks or boulders, the GTS has a large field-of-view (FoV), ellipsoidal in shape that will cover an area of roughly 100 m^2. The orientation of the FoV was selected to minimize direct heating of the observed ground by the rover, however, the area remains too close to rule out rover heating. This is made much worse by the orientation that JPL selected for Boom 1 that leads to significant thermal contamination of the ground viewed by the RTG.

Choice of Thermopiles Thermopiles were chosen as the IR detectors for the GTS because they are small and lightweight, and capable of functioning at almost any operating temperature applicable to Mars. Furthermore, they are sensitive to the whole IR spectrum, comparatively cheap and require only simple readout electronics, enabling further reductions to be made in the weight and size of the complete instrument. Finally, thermopiles can operate without the need for any sort of temperature control system, because they are less sensitive than other systems to the emergence of thermal gradients.

Thermopiles are not standard parts for space applications, however and at present no formally space-qualified thermopile sensors exist. Nevertheless, it should be noted here that the Infrared Thermal Mapper (IRTM) on the Viking orbiters and the MUPUS-TP experiment on the ROSETTA mission have demonstrated that thermopile detectors are well suited to measure low surface temperatures under spaceflight conditions. The thermopile model selected for the REMS is the TS-100, from the Institute for Physical High Technology (IPHT) in Jena (Germany), encapsulated within a TO-5 with no optical system but rather a thermopile filter built to specifications and pre-bonded onto the TO-5 as the thermopile window. The thermopiles have a non corrosive insulator and transparent N_2 atmosphere filling, as well as an internal RTD, a Pt1000, to measure temperature at the thermopile case base, which acts as a temperature reference for the thermocouple cold-junction.

Need for Inflight Calibration As the GTS is downward-looking, it is not expected that a high level of dust will be deposited on it, based on the experience of previous Martian optical instruments with similar configurations. However, it is not realistic to assume an *a priori* estimation of the degradation due to dust over the mission lifetime. To mitigate against dust deposition as the likely key source of degradation and hence to recover accurate ground temperature measurements, an in-flight recalibration system has been implemented. This system

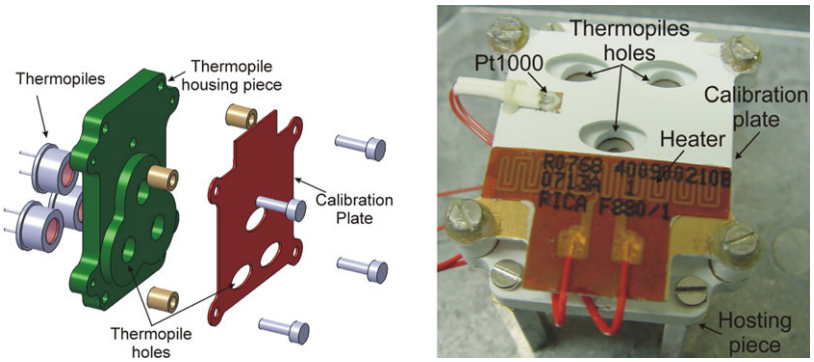

Fig. 5 *Left*: 3D mechanical layout of REMS GTS. *Right*: Picture of the REMS GTS flight model. (Credit: CAB (CSIC-INTA))

Table 4 GTS general characteristics (without electronics) and required performances

GTS property	Value
Dimensions	$40 \times 28 \times 19$ mm^3
Mass	20 g
Temperature working range (T_c) (Min-Max)	150–300 K
Ground temperature range	T_c ±40 K
Field of view (FOV)	60° (horizontal), 40° (vertical)

is based on a simple low mass and high emissivity calibration plate (Fig. 5), which can be heated to a given temperature and is placed in front of the thermopile housing piece, so that each IR detector looks at the ground through a hole in the plate. Thus, part of the FOV is obstructed by the calibration system, hence defining the measurement solid angle (Table 4). Indeed, the calibration plate system allows an estimate of the factors that influence the global sensitivity of the detectors to be determined and hence to correct GTS measurements over the mission. One thing that calibration cannot correct for is that continued dust deposition shall imply a directly proportional reduction of the signal to noise ratio for GTS, increasing sensor uncertainty (*e.g.* in the limit of complete dust obscuration the signal shall fall to zero and hence the measurement uncertainty shall rise to infinity even with perfect calibration).

The calibration plate is heated using an electrical heater consisting on an etched-foil resistive heating element laminated between layers of polymide, a flexible and thin insulator. Its temperature is measured using a dedicated RTD (Pt1000) attached to its surface. This recalibration system with no moving parts avoids complicated and costly commercial air purge systems to maintain the sensor window free of dust.

Spectral Response of the GTS Chanels The GTS uses three different thermopiles covering three different infrared wavelength channels, designated A, B and C (Table 5). The first two bands are optimized for the warmer and cooler portions of the Martian ground temperature range. Following Wien's law, the wavelength of maximum blackbody spectral radiance for a given temperature is given by $\lambda_{\max}$ [μm] $= 2898/T$ [K]. If the maximal and minimal Martian temperatures are 300 K and 150 K, then the sensor is designed to work optimally in the range from 9.9 μm to 19.3 μm. Additionally, the measurements must be performed within

Table 5 GTS thermopiles characteristics

GTS Item	Wavelength Sensitivity	Unit	Range Min-Max	Sensitivity Min-Max
Thermopile A (Group of thermocouples)	8–14 μm (average transmittance 75 %) see Fig. 6	Volts	±1.6 mV	35–70 μV/K
Thermopile B (Group of thermocouples)	15–19 μm (average transmittance 75 %) see Fig. 6	Volts	±0.64 mV	12–16 μV/K
Thermopile C (Group of thermocouples)	14.5–15.5 μm (average transmittance 75 %) see Fig. 6	Volts	±0.25 mV	4.7–6.6 μV/K

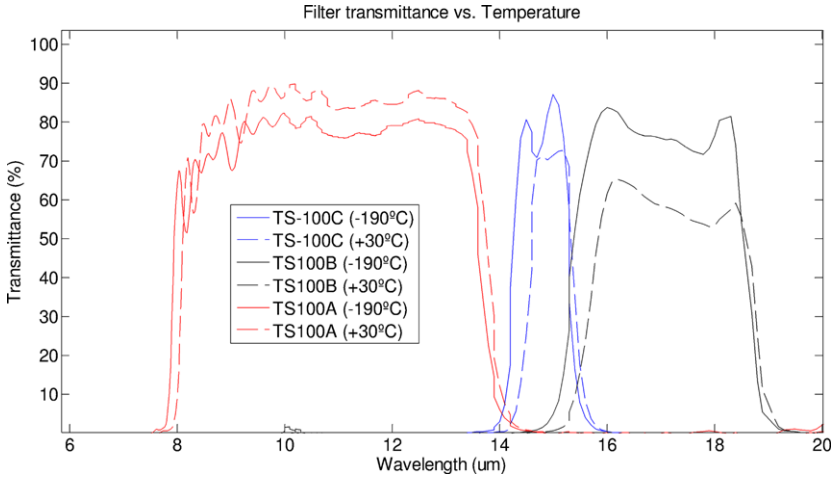

Fig. 6 Transmittance of the GTS thermopiles at different temperatures

a range where the ratio of IR radiance emitted by the Martian surface to the solar IR radiance reflected by the Martian surface, for typical Martian soil emissivities, is significantly greater than one. This condition is achieved above 8 μm, where the solar reflected radiance is smaller than 0.5 % for 150 K. Finally, the last restriction involved in the selection of these bands was to avoid the CO_2 atmospheric absorption band centered at 15 μm, with a bandwidth of 1 μm, that is the main component of the Martian atmosphere IR absorption/emission. Within this band gaseous atmospheric absorption can significantly alter the brightness temperature, even over the few 10's of meters path of the GTS. Indeed, a third GTS band is centered on the CO_2 absorption band. This allows any residual influence that the atmosphere may have on the other two thermopile bands to be determined and may allow the brightness temperature of the air at roughly 0.5 m above the surface to be retrieved, in analogy with the MER mini-TES experiment.

Effect of Surface Emissivity Uncertainty on Interpretation of GTS Measurements The measurement requirements for GTS are for 2 K resolution and 10 K absolute accuracy. Aside from the uncertainties within the GTS system, the choice of brightness temperature measurements to determine surface kinetic temperature contains its own uncertainty: we do not

know the surface emissivity (e.g. Kieffer et al. 1972; Daniel 1990). The choice of IR thermopile radiometery for GTS was based on results from the Mars Global Surveyor Thermal Emission Spectrometer (TES) and more recently and directly, the MER mini-TES results. In particular, mini-TES results suggest that surface emissivities at two Martian landing sites were generally at or above 0.95. Emissivities at or below 0.9 were very rare. These results are generally consistent with TES orbital observations. Orbital data suggest that the Gale Crater site will have a relatively high emissivity, above 0.95. Given that the ratio of kinetic surface temperature to brightness temperature is given by the inverse of the fourth root of emissivity, for emissivities of 0.85, 0.9, 0.95, and 1 the error for a 300 K surface is 12.4 K, 8 K, 4 K, and 0 K (4.1 %, 2.7 %, 1.3 %, and 0 % respectively). Given that the 0.9–1 range covers the vast majority of Martian surfaces, a retrieval assumption of 0.95 for emissivity introduces a centering of the error such that the spread shifts to 3.8 K, 0 K, 4 K, and 8 K (1.3 %, 0 %, 1.3 %, and 2.7 %, respectively). Since the FoV is large and the resolution is only relevant for repeated measurements at the same site, hence with the same emissivity, the emissivity uncertainly only influences the absolute accuracy. Hence, even for the unlikely case of anomalously low emissivity the induced error for absolute accuracy is below the 10 K requirement.

In fact, it is likely that information from other instruments and from laboratory experiments will help reduce the emissivity further. The emissivity is determined by the composition of the surface, both its mineralogy and the particle size distribution. In this light, the laboratory Fourier transform IR (FTIR) reflectance spectra of a set of selected astrobiologically significant minerals (including oxides, oxi/hydroxides, sulphates, chlorides, opal and clays) and basalt (as the main and most widespread volcanic Martian rock) has been measured (Martín-Redondo et al. 2009), taking into account different mixing amounts of minerals and covering the GTS spectral range. A set of minerals were selected for the experiments, from verified standards (SARM, NCS, USGS) and Mars analogs (e.g. Rio Tinto, Jaroso, Atacama): hematite, goethite, magnetite, jarosite, halite, smectite/montmorillonite and opal (all inerals that have been detected on Mars). The mineral composition was previously verified by XRD (Seifert XRD 3003 TT). Samples were cut into small pieces, ground in an agate mortar, and sieved to get a powder smaller than 45 μm (in accordance with the expected average size/mean diameter of Martian regolith dust). All mineral powders were dried in order to fit the Mars arid surface conditions before their final analysis using a Nicolet Nexus FT-IR (Thermo), using a Reflectance accessory (Praying Mantis Diffuse Reflection attachment, HARRICK). Binary and ternary mixtures were performed, covering different percentages and using basalt (BDR-2, USGS) as general matrix/groundmass for the mineral combinations. All spectra were recorded, covering the working wavelength range of the REMS GTS. The results obtained indicated significant percentage increases or decreases of reflectance in the whole wavelength range (e.g basalt-hematite vs. basalt-magnetite) and specific variations restricted to some spectral bands (e.g. basalt-smectite vs. basalt-opal). Data showed that the basalt reflectance percentage increases or decreases, even up to 100 %, depending on the mixing of the different minerals. This study confirms the necessity of taking into account the chemical-mineralogical assemblages (and textures) for any study and interpretation of Mars surface environment (e.g. its ground temperature), and that it will be necessary: (a) to incorporate new mineral phases (e.g. carbonates) and (b) to compare the results obtained in the laboratory with additional IR measurements, carried out directly on the field, on geological outcrops displaying different mineralogical associations. Significantly, it suggests that mineralogy and surface texture determined from other MSL instruments likely can be used to help reduce uncertainty in the emissivity and help improve the GTS absolute accuracy.

The GTS Instrument Thermal Model The thermal model for the GTS system is needed to determine the planetary surface brightness temperature from the various sensor measurements and to interpret the calibration plate results. It is based on an energy balance equation that accounts for the heat fluxes exchanged by radiation, conduction and convection between thermopile detector and the elements around, considering explicitly the sensor's internal and external physical structure and operation. Despite being more mathematically complex than that commonly used, this model has permitted the design of practical methodologies to compensate the effects of sensor spatial thermal gradients, and to calibrate model constants based on a differential approach.

The model starts from the definition of an energy balance equation (1) which accounts for the heat fluxes entering the thermopile bolometer from all the bodies around it, disregarding the heat fluxes between physical elements other than the bolometer (Fig. 7). The bolometer is designed to be well insulated from the thermopile case and to have low thermal mass, so that the following equilibrium condition is reached after a settling time of a few milliseconds.

$$P_{R,g-s} + P_{R,p-s} + P_{R,cc-s} + P_{R,cd-s} + P_{C,cb-s} = 0 \tag{1}$$

The terms $P_{R,x-x}$ and $P_{C,x-x}$ of (1) represent the heat power exchanged by radiation, and conduction and convection, respectively, whilst the subscripts x refer to the bodies that exchange the heat (g is for the ground, p for the calibration plate, f for the filter, cc for the thermopile case cap, cb for the thermopile case base and s for the bolometer). Based on simplified one dimensional heat transfer models (Sebastián et al. 2010), (1) can be expressed in terms of (2), assuming two reasonable simplifications:

- The temperature of the atmosphere inside the thermopile is equal to the temperature of the case base.
- The bolometer FOV, which is limited by the shape of the thermopile case, is equal to the sum of the bolometer FOV of the ground and the calibration plate FOV.

$$\begin{aligned} &\alpha K_1 \Phi_g + (1-\alpha) K_1 \Phi_p + K_1 \Phi_f + \frac{K_2}{2} \Phi_{cc} \\ &\quad + \frac{K_2}{2} \Phi_{cb} - (K_1 + K_2) \Phi_2 + K_3 * (T_{cb} - T_s) = 0 \end{aligned} \tag{2}$$

The constant α represents the factor of the thermopile FOV unobstructed by the flight calibration plate, whilst constants K_1, K_2 and K_3 group a set of physical constants such as areas, volumes, view factors, conductivities and convection coefficients. All of them are subject to calibration.

Meanwhile, the heat flux terms Φ_x are calculated using Planck's law, where $\times$ refers to the body. These terms depend on the transmittance of the thermopile filter, bolometer absorbance, and the temperatures and emissivities of the different bodies, such as the thermopile case base (T_{cb}) and calibration plate (T_p), which can be directly measured using the specific Pt1000 temperature sensors, the thermopile bolometer (T_s) and thermopile case cap (T_{cc}), which are measured indirectly as will be described below, and thermopile filter (T_f), which is assumed to be equal to the temperature of the thermopile case cap since they are in good thermal contact. Note that all the flux terms are known except for Φ_g, which is the unknown in the equation, and through its determination, the kinematic temperature of ground soil can be calculated.

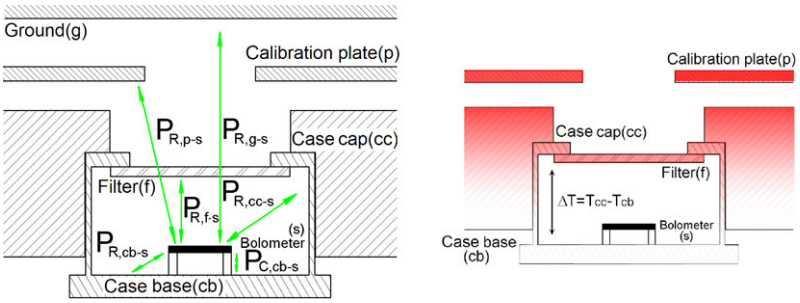

Fig. 7 *Left*: simplified diagram of GTS heat fluxes. *Right*: sketch of GTS and thermopile thermal gradient

The temperature of the bolometer, T_s, is obtained from the output voltage of the thermopile. The thermopile produces a voltage representation of the temperature difference between its case base (cold-junction) and the bolometer (hot-junction), (3). The GTS thermopiles have 100 thermocouples connected in series and embedded between the case base and the bolometer, and the term stands for the Seebeck coefficient related to the association of the two thermopile thermocouple materials.

$$V_{out} = 100\alpha_{AB}|_{T_c}(T_s - T_{cb}) \tag{3}$$

Finally, the temperature of the thermopile case cap, T_{cc}, is essentially the same as the temperature of the base, T_{cb}, since they are in good thermal contact. Nevertheless, the calibration plate, as is shown in Fig. 7, is screwed to the thermopile housing piece, creating a conductive thermal coupling between these two parts that extends to the thermopiles. In this way, small thermal gradients appear between the thermopile case cap, the top part, and the base or the bottom part, during the heating of the calibration plate. From this fact, a relationship between the overall temperature of the calibration plate and the temperature difference between the thermopile case base and case cap can be established (4). This relationship is assumed to be linear, its slope being given by the temperature-independent constant, K_{p-c}, which must also be determined experimentally/from calibration:

$$T_{cc} - T_{cb} = K_{p-c}\Delta T_p \tag{4}$$

In-flight Calibration Equations One of the main GTS priorities is how to resolve the gradual build-up of dust on the filters. In the course of operations on Mars dust will adhere to the thermopile filter. Dust has high emissivity and can block light into and out of the detector, and when in contact with the filter acquires the same temperature. Thus, dust can be seen as changing the area of the filter into something similar to the case, since thermal conduction dominates over radiation with the environment, and the sunlight does not hit directly the thermopiles. In other words, if we define a factor β representing that part of the FOV which has not been obstructed by dust, (2) can be rewritten as follows:

$$\begin{aligned}&\beta\alpha K_1\Phi_g + \beta(1-\alpha)K_1\Phi_p + \beta K_1\Phi_f \\ &+ \frac{K_2}{2}\Phi_{cc} + \frac{K_2}{2}\Phi_{cb} - (\beta K_1 + K_2)\Phi_s + K_3(T_{cb} - T_s) = 0\end{aligned} \tag{5}$$

Therefore, factor β must be determined during operations. This can be done by varying the temperature of the calibration plate through heating it up, whilst ground temperature remains stable. Thus, using (5) for two different calibration plate temperatures, the system

of equations (6) and (7) can be defined:

$$\beta\left[\alpha K_1 \Phi_g + (1-\alpha) K_1 \Phi_{p1} * c_1\right] + d_1 = 0 \tag{6}$$

$$\beta\left[\alpha K_1 \Phi_g + (1-\alpha) K_1 \Phi_{p2} * c_2\right] + d_2 = 0 \tag{7}$$

where

- $c_1 = K_1 \Phi_{cc1} - K_1 \Phi_{s1}$
- $d_1 = \frac{K_2}{2}(\Phi_{cc1} - \Phi_{cb1} - K_2 \Phi_{s1} + K_3(T_{cb1} - T_{s1})$
- $c_1 = K_1 \Phi_{cc2} - K_1 \Phi_{s2}$
- $d_2 = \frac{K_2}{2}(\Phi_{cc2} - \Phi_{cb2} - K_2 \Phi_{s2} + K_3(T_{cb2} - T_{s2})$

are a set of known heat terms, in which it is assumed that T_{cc}, T_{cb} and T_s may be different for each of the two calibration plate temperatures. Finally, the system of equations (6) and (7) can be solved for the factor β, eliminating the unknown but constant term $\alpha K_1 \Phi_g$ and depending only on measured temperatures and calibrated constants:

$$\beta = \frac{d_2 - d_1}{(1-\alpha) K_1 (\Phi_{p1} - \Phi_{p2}) + c - 1 - c_2} \tag{8}$$

An important consideration is that the value of β is not only affected by the deposition of dust, but also determined by the global sensitivity of the GTS. Therefore parameters such as the thermopile sensitivity and the ASIC channels gain modify their value, that initially after the thermopiles calibration will take an ideal unitary value.

Pre-flight Calibration The main priority of the REMS GTS calibration plan will be centered on the absolute calibration of the thermopiles detectors, since it is assumed a previous characterization campaign of GTS ASIC channels. This means to identify those unknown constants of the energy balance equation K_1, K_2, K_3, α, β and K_{p-c}. In addition to that, a set of auxiliary tests are required: The calibration of the RTD sensors associated to the thermopiles and the calibration plate. And the spectral characterization of the thermopiles filters transmittance and the calibration plate emissivity, that will allow the correct calculus of the heat flux terms, in the energy balance equation. Table 3 provides an overview and description of the GTS sensor calibration at different levels: Subsystem or detector level, and system or global sensor level.

The GTS calibration was performed at different levels: subsystem or detector level, and system or global sensor level. Hereinafter all the calibration tests are identified:

- Flight calibration plate emissivity determination. Performed at ambient temperature to obtain the emissivity curve of the flight calibration plate from 6 μm to 40 μm.
- Thermopile filter characterization. Carried out at nitrogen atmosphere with the filter at temperatures from 123 K to 313 K with intervals 10 K for characterizing the filter transmittance versus wavelength and temperature from 6 μm to 40 μm.
- Thermopiles-RTD and calibration plate-RTD characterization versus temperature. In the case, the test has been carried out in a cryostat from 98 K to 303 K.
- Thermopile-sensor characterization versus temperature. At thermal vacuum conditions and with the thermopile temperatures ranging from 123 K to 313 K, with intervals 10 K and finding the value of the constants of the energy balance equation K_1, K_2, K_3.
- Ground relative field of view. At thermal vacuum conditions also with the thermopile temperature at 313 K and obtaining the relative part of field of view not obstructed by the flight calibration plate α.

– Identification of thermopile thermal gradient constant K_{p-c}. In this case, the test was performed with Martian like atmosphere and ambient temperature. The relationship, K_{p-c}, between the increase in the calibration plate temperature and the thermal gradient generated between the thermopile's can cap and base.
– End to end calibration. Performed at laboratory conditions and therefore the thermopile was at ambient temperature. The goal was to find the initial value of β. Its value may have changed as consequence of the Boom 1 environmental test campaign.

The experimental setup of electro-optical calibration GTS 4 and GTS 5, see Fig. 8, consists on a large area blackbody calibration source, and a cryostat where the GTS is located in order to change the thermopile temperature covering the Martian working range. The thermopile faces the radiation surface of the blackbody through the cryostat IR window made of KRS-5.

For tests GTS 6 and GTS 7 the GTS will be integrated in the REMS boom 1, using ASIC electronics as readout system. In both tests temperature change is not required, thus the cryostat is not used. In test GTS 6 a specific chamber has been designed for creating Martian like atmosphere conditions and acting as blackbody surface at ambient temperature, while for test GTS 7 the GTS will be directly confronted to the blackbody.

Differential Process for GTS Model Identification In order to avoid the uncontrolled but constant heat flux terms derived from the experimental test setups, see as example Fig. 8, differential procedures and analysis of the energy balance equation have been applied. These undesired terms are: the blackbody environment reflections Φ_r, that arise because blackbody emissivity is different from one, and the IR window emissions and reflections. These heat flux terms appear in the energy balance equation (5), modifying it until it is converted into (8), where χ_w represents the cryostat window average transmittance.

$$\beta\alpha K_1(\chi_w\Phi_g + \Phi_w + \Phi_r) + \beta(1-\alpha)K_1\Phi_p + \beta K_1\Phi_f + \frac{K_2}{2}\Phi_{cc} + \frac{K_2}{2}\Phi_{cb} - (\beta K_1 + K_2)\Phi_s + K_3(T_{cb} - T_s) = 0 \quad (9)$$

The differential procedure combines two energy balance equations 9 for pairs of blackbody or calibration plate temperatures with the same thermopile temperature. Thus, by subtracting the two energy balance equations, in which the temperatures of the cryostat IR window and the laboratory environment remain stable, the unknown but constant heat flux terms Φ_r and Φ_w, are eliminated. A detailed analysis of this procedure can be found in Sebastián et al. (2010). Additionally, the differential procedure makes it possible to avoid errors caused by the constant thermal gradients on each thermopiles can, which may appear for each consigned thermopile temperature as the thermopiles hosting piece is heated or cooled (Sebastián et al. 2011).

4.3 Air Temperature Sensor

The air temperature sensors (ATS) are critical for REMS science goals, in particular for studies of the PBL convection processes and water cycling. The observational requirements are: temperature measurements within the interval 150–300 K (to cover a wide range compatible with any landing site and season), with an absolute accuracy of at least 5 K, and a resolution of 0.1 K. The latter requirement stems from the goal of measuring subtle temperature changes across dynamical features such as fronts, convective cells and dust devils. Since direct eddy correlation will not be attempted, sensor sampling rates of better than 1 Hz

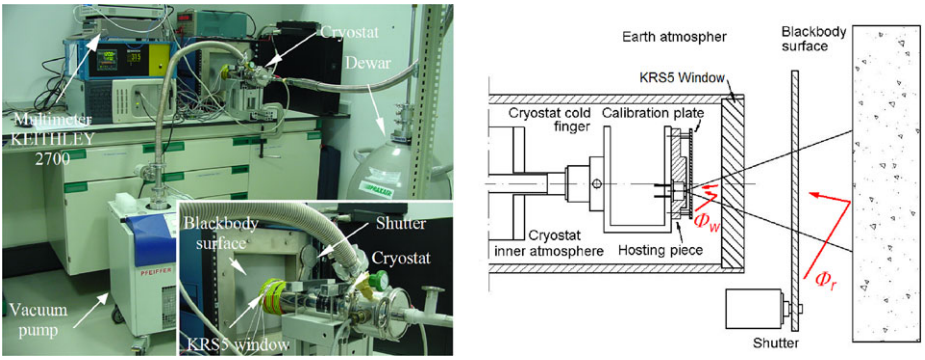

Fig. 8 *Left*: GTS calibration experimental setup. *Right*: sketch of the setup showing undesired flux terms. (Credit: CAB (CSIC-INTA))

are not needed. Therefore the ATS design was based on the use of thermistors because of their robustness in spite of their lower response time.

The REMS ATS sensors need to measure a temperature representative of the local environment even when subjected to thermal influences such as heat conduction through its support to the boom, thermal boundary layer effects of boom and mast, direct solar irradiation of the sensor, and rover thermal contamination through radiation and convection. In the sensor design and the adapted retrieval algorithm the contamination of those effects is avoided. Finally, the ATS design reflects additional constraints in terms of the need to be sufficiently robust to assure survival during MSL entry, descent and landing and to satisfy the severe mass, power, physical envelope and data allocation restrictions imposed on the scientific payload.

The REMS ATS sensor consists of a 35 mm long thin fin manufactured with a multilayer of FR4, with two Minisens RTD thermistors, of type PT1000 Class A, of 1.2 mm × 1.6 mm size. The PCB traces that transmit the electrical signals from the sensor to the ASIC electronics are printed on the surface of the fin (see Fig. 9). These traces are 17 μm thick and 0.25 mm wide and are printed in a zig-zag pattern to minimize the heat conduction from the ASIC and boom to the thermistors. The two PT1000 sensors are bonded to the tip and at intermediate position. In addition the temperature at the base is monitored by an independent thermistor of the boom. Thus the REMS-ATS algorithm uses three RTDs: at the base T_b, an intermediate point T_{Ln} and the tip T_a. With REMS ATS one can estimate simultaneously the temperature decay profile (which depends on the instantaneous convection-conduction scenario) and the fluid temperature despite the thermal contamination due to the boom and radiative forcing.

Air Temperature Retrieval The ATS temperature retrieval model is based on the thermal physics of a thin fin in equilibrium with the fluid around it. This profile depends on: conduction through the FR4 material and electrical wires; local convection (natural and forced) within the Martian atmosphere which in turn depends on the temperature difference between the beam and the fluid, the geometry, the wind speed, atmospheric pressure and gas mixing coefficients; the IR radiative interchange between the beam and the air around it which is also dependent on the temperature difference between the beam and the fluid temperature, the IR emissivity (which changes due to dust deposition); the solar radiative heating (mostly in the visible range) which changes with season and time, atmospheric absorption and emissivity and partial shading due to the booms for certain angle of incidences. The temperature

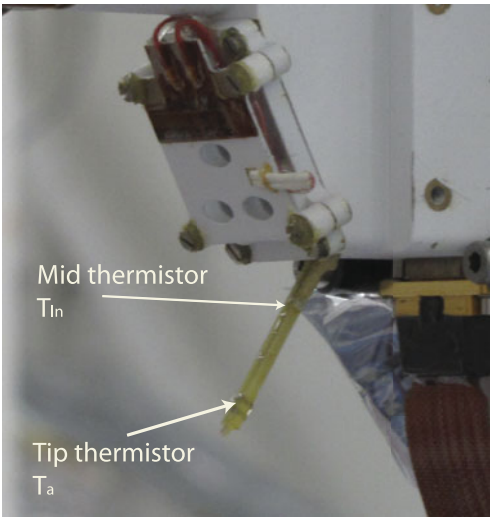

Fig. 9 Image of the ATS implementation on the Booms 1. ATS sensors are composed of a multilayer FR4 rod 35 mm long with two PT1000 Class A thermistors. One of them is located at the tip of the rod and the other at an intermediate position. Both RTDs are wired internally. (Credit: NASA/JPL)

retrieval obtains the temperature of the fluid T_f using three known temperatures of a fin (T_b, T_{Ln}, T_a) which is attached to a large thermal mass. For a given fluid temperature T_f, and fixed base temperature T_b, the temperature difference at position x in the fin $\theta = T_x - T_f$, is given by:

$$\frac{d^2\theta}{d\chi^2} - m^2(\chi, \theta, T_f)\theta = 0 \tag{10}$$

$$\theta|_{\chi=0} = \theta_b \tag{11}$$

where $\chi = x/L$, $m = L\sqrt{4 * (h_{conv} + h_{rad})/(kD)}$ and h_{conv} the local convection term, $h_{rad} = \varepsilon\sigma(T_x^2 + T_f^2)(T + T_f)$ the local radiation term, ε the IR emissivity of the fin material, σ the Boltzman constant, k the fin conductivity constant and L and D the length and diameter of the cylinder respectively. The value of h_{conv} can change depending on the geometry and the characteristics of the fluid, however its exact dependency does not matter for this temperature retrieval algorithm (Mueller and Abu-Mulaweh 2006).[2]

The same applies to the exact conductivity or IR emissivity of the fin. Knowledge of the exact values of these parameters is not needed for this measuring concept. Instead, and by using the three simultaneous temperature measurements provided by the RTDs, the algorithm provides an average ratio of all these values together with the air temperature.

Assuming that the heat transfer out of the fin tip is negligible $\frac{dT}{d\chi}|_{\chi=1} = 0$ and if the fin is assumed to have a uniform convection term then this system has an exact solution:

$$\theta(\chi) = \theta_b \frac{\cosh \overline{m}(1-\chi)}{\cosh \overline{m}} \tag{12}$$

[2] In particular, the natural convection term can be described by $h_{conv}^{free} = \frac{0.36k_f}{D} + \frac{0.518k_f(g\beta/\nu\alpha)^{1/4}}{(1+(0.559/Pr)^{9/16})^{4/9}} \frac{\theta^{1/4}}{D^{1/4}}$. In the case of forced convection (if $RePr > 2$) then for a cylinder $h_{conv}^{forced} = \frac{k_f Nu}{D}$ with Nu the Nusselt number: $Nu = 0.3 + 0.54Re^{1/2}Pr^{1/3}(1 + (Re/28200)^{5/8})^{4/5}$ and $Re = \frac{v_{wind}D}{\nu}$ the Reynolds number.

where $\overline{m} = L\sqrt{\frac{4\bar{h}}{kD}}$. Here a bar over a quantity denotes average value over the length. This model of the temperature along a thin fin cooled by natural convection and radiation has been validated experimentally by Mueller and Abu-Mulaweh (2006), and is the starting point of REMS-ATS novel design and retrieval method.

Assuming that we measure the temperatures at the base of the fin T_b ($x = 0$), at the free end T_a at $x = L$ and at an intermediate point at $x = L/n$ where the temperature is T_{Ln} then at equilibrium:

$$(T_a - T_f) = (T_b - T_f)\frac{1}{\cosh \overline{m}} \tag{13}$$

$$(T_{Ln} - T_f) = (T_{Ln} - T_f)\frac{\cosh \overline{m}(1 - \frac{1}{n})}{\cosh \overline{m}} \tag{14}$$

Solving this system of two equations we can obtain the two unknowns: T_f and $\overline{m}$ simultaneously. The temperature obtained by doing this, T_f, is free from rover and solar heating contamination and shall be given as ATS temperature, since REMS has one ATS sensor in each boom there will be an ATS 1 and ATS 2 temperature reading.

This mathematical model has been confirmed accurately with an engineering model of the ATS at a Martian chamber facility at the Centro de Astrobiología (CAB), under a variety of environmental conditions under Martian pressure (with different scenarios of wind intensity, boom and environmental temperature) and in field (terrestrial) measurements under varying conditions of solar insolation and wind. As result of this calibration the rms of error of the ATS compared with an external reference temperature was shown to be 1 K (not shown). The details of this validation will be published elsewhere.

Retrieval Performance During a Rover Thermal Test We include here, as example of the REMS ATS retrieval process under nominal operation conditions, the end-to-end validation of the ATS flight model and retrieval process once assembled on the rover. These data were taken during the System Thermal Test (STT) performed at JPL during the final rover assembly tests. The tests were run within an environmental chamber at Martian pressure with an almost fully operational rover, with all its instruments operating, including a device emulating the heating generated by the RTG. The Solar lamps of the Martian chamber were adjusted to different levels of intensity to emulate the radiative forcing during the solar cycle on Mars and the thermal diurnal cycle of the air was emulated by injection of N_2 at different temperatures. A set of wire-hung thermocouples (T_c's) were used to monitor the ambient temperature in the vicinity of the rover. The temperature sensed by the T_c's is free from solar heating contamination, because of the small size of the T_c's, and from rover conduction contamination because they were hung from wires and were not directly connected to the rover. An average of the temperature sensed by the two T_c's that were placed on either side above the rover mast shall be taken as the reference temperature for the air. At the beginning of every hour, REMS performed its nominal acquisition of measurements at 1 Hz. Since the air temperature was modified by N_2 flow, the temperature around the rover may be not have been uniform as it depended on the flow of the injected cool N_2 and the contamination induced by the rover. Two examples of the results of this test are shown in Fig. 10, where part of the diurnal temperature cycle is seen. The reference T_c's provide a temperature measurement every minute. The ATS sensor, at 1 Hz, is able to provide accurate temperature measurements in spite of rover and solar contamination confirming the robustness of REMS ATS retrieval concept. The sensor is sensitive also to quick temperature oscillations.

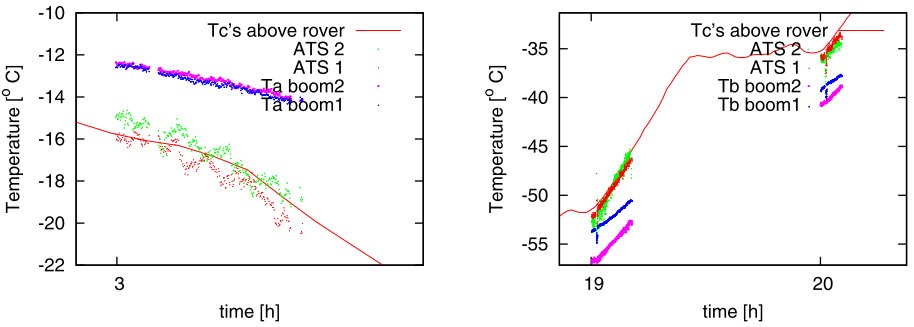

Fig. 10 Detail of the ATS end-to-end validation in a full Martian diurnal cycle during final assembly testing at JPL Martian chamber. The full test consists of a 25 hours long diurnal cycle, starting and ending at maximal solar incident power and air temperature, with ambient temperatures ranging between −75 °C and 0 °C, under Martian pressure conditions and with radiative forcing emulated by Solar lamps. The temperatures provided by the ATS retrieval model (ATS 2 and ATS 1) are compared with the reference ambient temperatures of the T_c's. For completeness the measured temperatures sensed at the tip, T_a, or the base, T_b, of the ATS fins of either boom are included. (*Left*) REMS-ATS 1 Hz measurements during the first five minutes of one of the hours of maximal solar irradiance. The T_a's are roughly 5 °C warmer than the air. (*Right*) REMS-ATS 1 Hz measurements during the first fifteen and five minutes of two of the hours of weak solar irradiance, as the temperature rises after the long cold hours of night. The T_b's are between 5 °C and 1 °C (depending on the boom and its ASIC temperature) colder than the air. In either case, the retrieval model obtains the temperature of the air correctly. (Credit: CAB (CSIC-INTA))

Air Temperature Sensor Calibration In reference to the ATS retrieval model, the calibration has two steps: (i) calibration of temperatures transducers (thermistors) and (ii) computation of models errors at different $\overline{m}$ conditions (see (13)) and time response.

The measurement chain of each thermistor is determined by the sensor and electronics conditioning (amplifier and analog-digital converter (ADC)) located in the Boom ASIC's, and the goal is to relate resistance changes with ADC output counts.

$$CountsReading = Gain \times Resistance_{Pt1000} + Offset \tag{15}$$

In REMS, the Offset depends on the ASIC temperature as well as the ASIC power supply voltage, Ground Temperature Sensor (GTS) gain (only for Boom 1) and Wind Sensor (WS) status, as it has been highlighted during calibrations testing. The gain has also a dependence on the ASIC temperature. An intensive testing campaign of the flight hardware has been carried out to determine those relationships.

Each thermistor has been calibrated independently to determine its resistance variation with temperature. With that function and (15) it is possible to determine the temperature from (13). The accuracy of the thermistors temperature (not to be confused with the ATS global accuracy in determining the air temperature free from contamination) is better that 0.01 K and the ATS global accuracy could be improved further by applying a filtering process.

For the second step, a series of tests have been performed under ambient, vacuum (TVT chamber) and Martian atmospheric conditions to verify instrument functional performance, including end-to-end performance determination and to estimate the rms error and response time under varying $\overline{m}$ conditions.

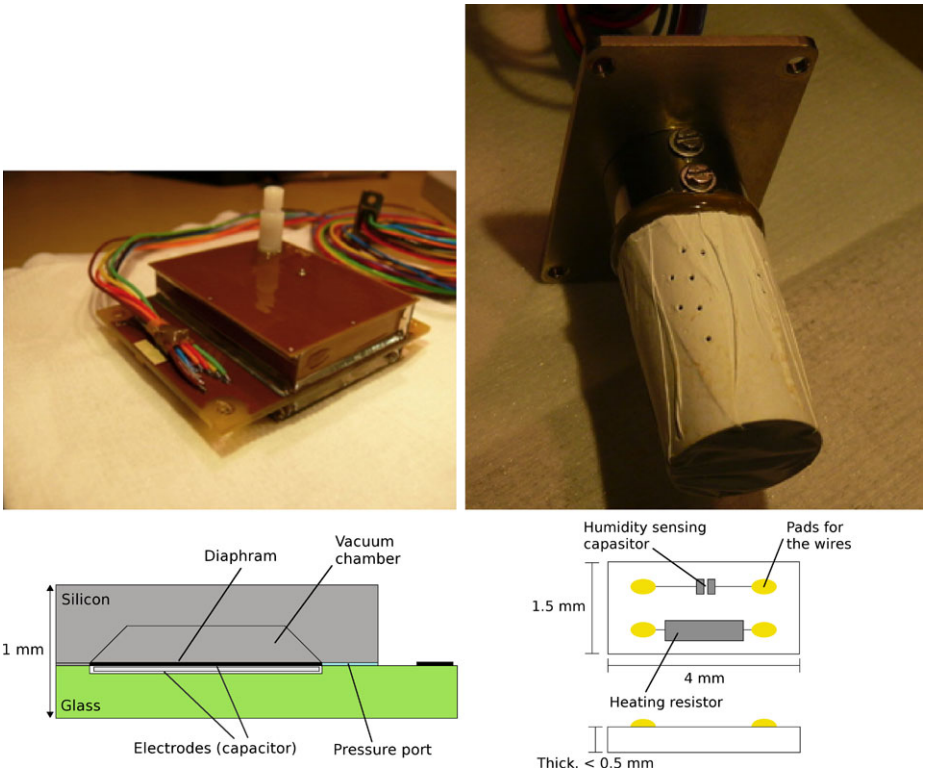

Fig. 11 *Left*: picture of the Pressure Sensor and conceptual sketch. *Right*: same information for the Humidity Sensor. (Credit: FMI)

4.4 Pressure Sensor

The Pressure sensor makes use of two transducers placed on a single multi-layer PCB (see Fig. 11) of a 62×50 mm^2 size and protected by box-like FR4 Faraday cages. The sensor resides inside the REMS ICU box. The transducers of the Pressure sensor can be used in turn, thus providing some redundancy and improved reliability. Each transducer has 2 Vaisala Barocap® pressure sensor heads and 2 Thermocap® temperature sensors. The Barocap® sensor heads are of different types: 1 is of high-stability, and 3 are of high-resolution type.

The Barocap® sensor head is a single-crystal silicon micromachined device, therefore its intrinsic stability is extremely good. The measurement is based on capacitor plates (electrodes) moved by pressure, thus changing the capacitance of the sensor head. The nominal capacitance of a Barocap® at Mars is between 10 and 15 pF depending on its type. Similar pressure heads as used by REMS have been utilized in the highly successful Huygens/Cassini mission at the Saturnian moon Titan as well as by Phoenix Mars mission (Harri et al. 1998a, 1998b, 2006; Taylor et al. 2008, 2010).

4.5 Pressure Sensor Calibration

The pressure sensor is calibrated by measuring its output in several pressure and temperature points under stable and changing temperature. The stable temperature measurements are

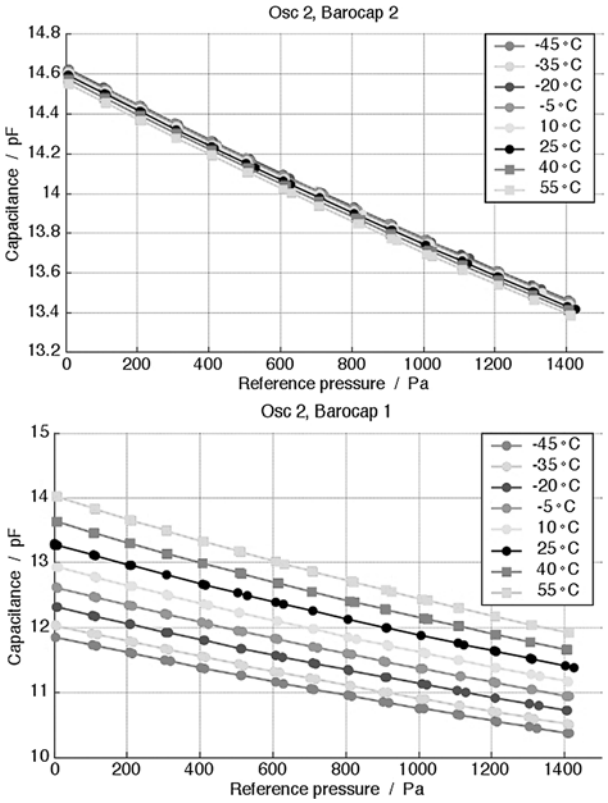

Fig. 12 Pressure sensor calibration results. *Upper plot*: capacitance response versus pressure at different temperatures for the high resolution head. *Lower plot*: capacitance response versus pressure at different temperatures for the high stability head. (Credit: FMI)

performed over the range of 0–14 hPa (vacuum to Martian pressure range) with 100 Pa intervals and −45 °C…+55 °C (operational temperature range inside REMS ICU box) with max 15 °C intervals. In the measurements under changing temperature pressure is kept in 8 Pa while temperature is swept over the operational range down and up with rates ±15 °C/h and ±30 °C/h. A Vaisala PTB201 pressure transmitter modified for the Martian pressure range is used as pressure reference. The accuracy of the reference sensor is 1 Pa and the calibration is traceable to national standards. Figure 12 depitcs typical calibration curves, where is shown the linearity of the high resolution and high stability head at different temperatures.

The data of the temperature sweep measurements is used for compensating the "thermal lag effect" that caused notable deviations in the data of the Phoenix pressure sensor before its mathematical compensation (Taylor et al. 2010). In REMS this compensation algorithm is a part of the data processing pipeline. Changes in ambient temperature also cause slowly evolving temperature hysteresis, the magnitude of which depends on the magnitude and rate of the temperature variations. In "Day in life" scenario in the MSL System Thermal Test, the temperature of the Pressure sensor varied from +10 °C to +33 °C during one sol and the fastest temperature change rate was 6 °C/h. Corresponding short-term variation in the reading of the high-stability Barocap is less than 1 Pa peak-to-peak, and in the worst case scenario it would be 2 Pa peak-to-peak.

Another phenomenon that affects the readings of the Pressure sensor is water in- and outgassing of the Barocap® sensor heads. During the storage in ambient pressure, water is condensed in the sensor heads changing their temperature dependence. When the pressure is

lowered and/or the sensor is heated, the water outgases. This has been taken into account in on-ground tests and calibrations by giving the sensor enough time to outgas warm temperature and in low pressure before measurements. Based on experience from the Phoenix pressure sensor the water in-gassed during pre-launch storage may not outgas completely during the interplanetary cruise. Consequently, outgassing during the surface operations phase may still change the temperature dependence of the Barocap®. The time scale of this uncertainty is one sol and the magnitude for the high-stability Barocap® is estimated to be less than 1.5 Pa peak-to-peak during the most of the mission. During the first few weeks after landing the magnitude might be stronger as a consequence of moisture outgassing.

Aging affects slightly the offsets of the pressure readings of the Barocap®. This effect can be almost fully compensated by subtracting a pressure value measured in vacuum from the readings in other pressures. The offset of the high-stability Barocap® stayed constant with ± 2 Pa precision during the whole test campaign. Also the offset of high-resolution Barocap® #2 stayed constant with ± 2 Pa between the last check-out in May 2009 and MSL System Thermal Test 22 months later, if kept under $+55$ °C temperature. Taking into account the accuracy of the reference sensor and the shown stability of the Barocap® during the test campaign, the absolute accuracy of daily averaged readings of these two Barocap® is 3 Pa after the first weeks of the mission, when most of the moisture has outgassed. The EOL accuracy will potentially be slightly worse, taking into account possible systematic drift with rate max 1 Pa/year. Offset drift is the only error source affecting daily averages as the deviations caused by other error sources average out.

The warm-up behavior of the sensor is such that there is an uncertainty in the readings measured right after power-up. The uncertainty decreases exponentially with time with the following time constants: 2 minutes for high-stability Barocap®, and 15 s for the high-resolution Barocap®. Thus the readings measured in the end of each 5-minute session are more accurate than the readings measured in the beginning, and they should be used in studies of long-term phenomena instead of the averages of the whole 5-minute sessions.

Based on the above effects, the Pressure sensor calibration is based on a number of tests, some of them for calibration purpose and other one for checking out, the list is the following one:

- Temperature calibration.
- Calibration 1. Verify the sensor's operation in the designated temperature and pressure area, calculate calibration coefficients and determine the short term repeatability of the sensor. This test also checks noisiness (resolution) and warm-up time and verifies that the sensor units are vacuum-proof. Measurements are performed during temperature changes to check the impact of changing temperature on the accuracy of the sensor.
- Check out tests. After the bake out environmental test and after thermal vacuum tests.
- Calibration 2. This second calibration test is performed after all instrument level environmental tests.
- Time response test.
- Random check data measurement.
- Input voltage test. The dependence on input voltage of the pressure readings of all Barocap channels.
- Temperature response test. Check the impact of changing temperature on the accuracy of the sensor.

4.6 Humidity Sensor

The Humidity sensor transducer includes 3 Humicap® sensor heads and 1 Thermocap®. The transducer electronics and the sensor heads are placed on a single multi-layer PCB

of a 36 × 15 mm^2 size protected by a metallic Faraday cage. The PCB is supported by a mechanical interface mounted on the REMS Boom. The Faraday cage is perforated to allow sufficient ventilation. The holes are covered with a PTFE filter material to protect the sensor head from dust (see Fig. 11).

The Humicap® sensor heads contain an active polymer film that changes its capacitance as function of relative humidity, with 0 to 100 % RH measurement range. The film reacts to the relative humidity, even if the instrument is not powered. Once powered, the relative humidity can be read almost immediately (1 s is allowed for electronics stabilization). Nominal capacitance of Humicap® is in order of 6 pF. The dynamic range of the Humicap® changes with temperature, being approximately 1 pF around 0 °C and ∼0.3 pF around −70 °C. The Humicap® also becomes logarithmically slower with lower temperature, its time constant is ∼0.1 s at +20 °C, but for example at −40 °C it is ∼30 s and at −70 °C ∼700 s. The time lag is about 5 min around −60 °C. The timelag can be mathematically partially compensated on-ground. The Thermocap® temperature sensor heads have no time lag.

The Humicap® sensor heads also have Pt heating resistors that are used periodically to heat the sensor heads to +135 °C...150 °C to eliminate possible contaminants that can affect the capacitance. This is called regeneration of the sensor. Regeneration consumes about 0.5 W during 5 min period.

4.7 Humidity Sensor Calibration

Three pieces of the Humidity sensor device were calibrated simultaneously: flight model, spare model and reference model. All 3 models were manufactured at the same time from the same material and component lots, and their properties are very close to each other. The purpose of the reference model is to study aging of the humidity sensor and to make reference measurements when needed.

The Humidity sensor calibration has been performed in two steps:

- Temperature calibration. Calculate calibration coefficients of the sensor heads and measure the resistance of the resistors.
- Humidity calibration: dry point, basic calibration, higher temperature range, lower temperature range.

The Humidity sensor calibration is performed by first calibrating the Thermocap® temperature sensor. Temperature calibration is done in at least 8 stable temperature points in a climate chamber. To get the most accurate results, the stability criteria for the climate chamber temperature is $\Delta T < 1°$/h and <0.1 °C during the measurement. Pt100 sensors attached directly to the instrument are used as reference sensors in the temperature calibration. These Pt100 sensors are in turn calibrated in a temperature calibration bath, the reference sensor of which is calibrated at Finnish Metrology and Accreditation Center and is traceable to national standards. As the result of the temperature calibration, ±0.1 °C accuracy compared to the Pt100 reference sensor is achieved for the Thermocap®.

At the same time with Thermocap®, also the heating resistor used for regeneration is calibrated against reference Pt100. ±0.1 °C accuracy is achieved also here. After temperature calibration, the Humicap® sensor head readings are measured in dry (∼0 % RH) and wet (∼100 % RH) conditions in 6–8 temperature points, at least 5 of which are below 0 °C. The lowest temperature point for humidity calibration is −70 °C. Dry conditions are achieved in a vacuum chamber and wet conditions in a closed vessel with substantial humidity, which is then cooled down until dew/frost point is achieved.

Humicap® behavior is linear (see Fig. 13 in terms of both temperature and humidity (ref: Vaisala)). As the result of dry and wet point measurements in different temperatures and

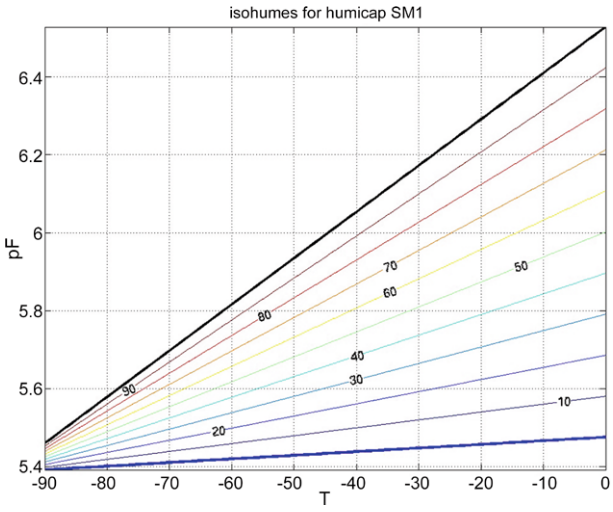

Fig. 13 Isohumes obtained during the HS calibration tests. (Credit: FMI, Sini Merikallio)

Humicap® linearity, isohumes of relative humidity in different temperatures can be calculated. Relative humidity can be found as a function of Humicap® capacitance and accurate temperature as measured by Thermocap®.

The calibration of the sensor is verified by measuring arbitrary humidity points in arbitrary temperatures. In temperatures above −40 °C the results are compared against Vaisala humidity and temperature transmitter HMT334/337. These devices are calibrated at Vaisala in accredited calibration laboratory and their calibration is traceable to national standards. In temperatures below −40 °C (down to −70 °C) the reference humidity is calculated based on readings from Vaisala's DM500 precision SAW hygrometer capable of measuring dew point temperatures with 0.2 °C accuracy down to −75 °C, and accurate temperature measurements with Pt100 reference sensors.

The Humidity sensor measures the relative humidity directly on the sensor surface. During the first couple of minutes of operation the sensor heats up about 1.5 °C that would lead to a considerable difference with the actual ambient humidity. Hence the first 5 to 10 humidity readings measured just after power-up while the temperature of the sensor is roughly the same as of the ambient are the most accurate (as stated in Sect. 4.6, the Humicap® sensor heads react to humidity changes even when the instrument is not powered). Heating of the sensor will be remodeled after some data from ground measurements on Mars have been received, after which the temperature difference can be compensated.

4.8 Wind Sensor

The Viking Meteorological Instrument System (VMIS) was the first meteorological package (including wind speed and direction sensors), to retrieve data from Mars during several years (Tillman et al. 1993). Mars Pathfinder followed it, landing on Mars in 1997 with a sensor suite which included a wind sensor too (Seiff et al. 1997). More recently, the Phoenix Mars lander reached Mars in 2007 equipped with a very simple windsock design (Taylor et al. 2008). Mars Polar Lander and Beagle 2 Lander, launched in December 1999 and June 2003 respectively, were designed to also measure wind speed and direction.

Hot wire anemometry was used in the Viking mission and from then, has been a reference in the design of wind sensors for Mars due mainly to its simplicity. The wind sensor

assembly in Viking 1 and 2 consisted of two hot wires oriented at right angles to each other. A reference air temperature was measured using an identical hot wire located between the two wind sensors. A quadrant sensor at the top of the assembly provided the wind direction. Finally, air temperature was measured independently using a thin wire thermocouple (Chamberlain et al. 1976). Three small aluminum windsocks were included on the Mars Pathfinder meteorological boom. The windsocks were mounted at different heights (0.53 m, 0.82 m, and 1.12 m above ground) in order to return information about the near-surface wind profile (Seiff et al. 1997). The Phoenix mission carried the 'telltale' also based on the dynamic pressure exerted on a thin kapton tube, which retrieved very coarse wind speed information (Taylor et al. 2008).

REMS follows Viking design and uses thermal anemometry to record the wind speed also. Hot wire anemometry is based on recording either the amount of power required to heat a wire so that it maintains a constant temperature difference with the ambient (CTA) or to record the temperature of the wire when supplied with a constant amount of power (CPA). The convective power is then calculated, which in turn is used to obtain the wind speed. The REMS wind sensors use a thin film instead of a wire: titanium thin film resistors patterned on the surface of a silicon chip (Domínguez et al. 2008).

In all previous missions, an arm or mast isolated the wind sensor from the lander body. However, this solution was not implemented in the MSL rover (see Sect. 4) and thus REMS wind data will be strongly influenced by the rover body and some of its appendages (e.g. masthead, RTG, robotic arm). CFD simulations have confirmed the effect of the perturbation by the rover on the sensor. Figure 14 presents the results of a simulation showing that there are large areas perturbed by both the mast and the rover body, highlighting the challenging task of the REMS WS to measure the background wind speed and direction away from the rover.

Flows around a cylindrical shape have been studied extensively in aerodynamics for many types of aircraft bodies. It is generally understood that when a fluid flows around a cylinder there is a zone where the stream is detached and another in which the fluid follows the shape of the body with a stagnation point in the hitting zone. This is the underlying idea behind the REMS wind sensor cylindrical design.

The velocity field in the vicinity of the surface of a cylindrical body is a function of the fluid properties, the geometry of the flow and the free flow speed. In particular, for the flow around a semi-infinite cylinder we can write:

$$\overrightarrow{V} = F(U_\infty, \theta, \phi, \mu, \rho, D, r, d) \tag{16}$$

where $\overrightarrow{V}$ is the local speed, U_∞ is the free flow speed, θ and ϕ are the incident and azimuth angles (see Fig. 16), D is the cylinder diameter, r is the radial distance from the cylinder axis to the point under study and d is the distance of the point to the end of the boom. μ and ρ are the air viscosity and density. Equation (17) shows the same equation but in its dimensionless form.

$$\overrightarrow{V}/U_\infty = F(Re, \theta, \phi, r/D, d/D) \tag{17}$$

The local speed at a certain point is a function of the Reynolds number (Re), the incident angles, its position with reference to the cylinder surface (r/D) and its distance to the boom tip (d/D). The REMS WS is designed to estimate U_∞, θ, and ϕ measuring two estimators of the local speed components at three points close to the cylinder surface.

In order to understand the flow around the REMS booms and also to assess the retrieval method CFD simulations were performed with the program EFDLab. Figure 15 shows some

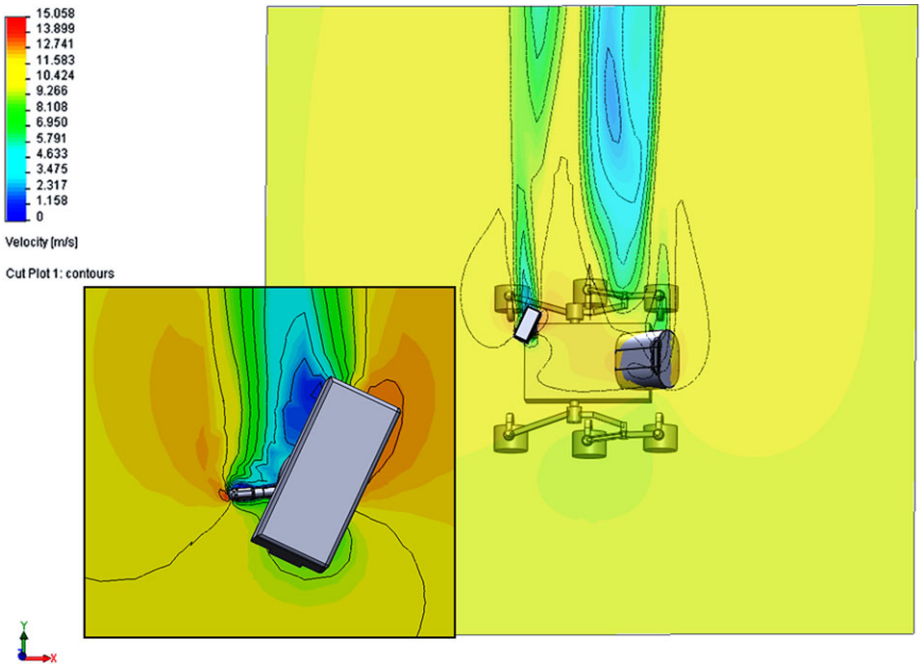

Fig. 14 CFD simulation of the MSL rover. Wind flows at 10 m/s from yaw $= -90°$. The simulation is run at $T = 273$ K and Pressure $= 7$ mbar. The horizontal plot is cut at height 39.3 cm above the rover deck (boom 2 axis) and includes a zoom of the area nearest to the booms. A vertical cut plot at the mast section is included below

results of these simulations. The main conclusions drawn from the study of the fluid movement are:

- The flow very close to the boom surface is almost two dimensional. As is expected for boundary layer flow, the component perpendicular to the surface is negligible.
- With three recording points making an angle of 120°, at least two of them will be outside the separation region for most incident angles. This has motivated using hot dice on boards disposed in a triangular geometry around each boom.
- As expected, the thickness of the momentum boundary layer is a function of Re. With higher Re the boundary layer becomes thinner. The local speed and angle dependences are not correlated.

In consequence one can rewrite (17) as:

$$\overrightarrow{V_i}/U_\infty = G(Re, r/D, d/D)H(\theta, \phi) \tag{18}$$

These considerations led to a REMS wind sensor concept, based on two booms at 120 degree from each other. Each boom records the local 2D speed at three boards on the boom surface. Each board is oriented at 120° from the next, and the combined reading from those boards determines the wind speed and upwind direction.

Local Wind Speed Estimators Each recording board is a bi-dimensional hot film anemometer consisting of four hot dice and a cold one on a transducer board as shown in Fig. 19. Each

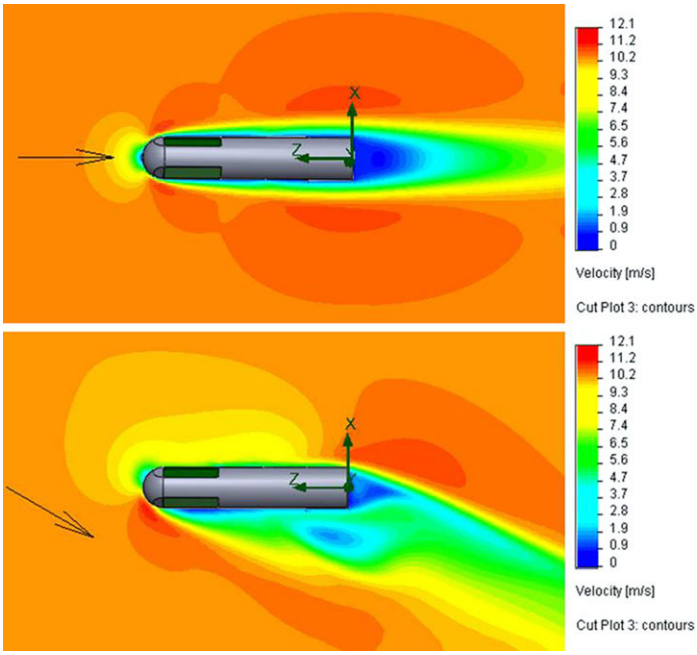

Fig. 15 Simulation of the boom model at different yaw angles. These results are used to be compared with real tests in the INTA Mars Linear Tunnel. The fluid was CO_2 at 298 K and 72.8 mbar, with wind at 1 m/s. The *top image* represents a stream in the boom axis direction (yaw = 0°), showing a speed field with the same symmetry as the boom. The *lower image* represents a 30° incident fluid, in this case it is clear how one board is in the wake area, whilst the other one will see record the wind movement

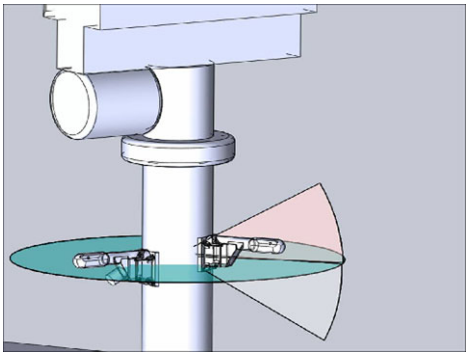

Fig. 16 Diagram showing the incident angles: Vertical angle is pitch, and the yaw angle indicates the wind direction

die has resistors to heat itself and to measure its own temperature. They are isolated from the board by four pillars with a low thermal conductance material. These dice are assembled in a square configuration and kept at a fixed temperature difference with respect to a cold die (located further apart) using an individual electro-thermal sigma-delta control loop that supplies power to each hot die. The four dice electronics concept is described in detail in Domínguez et al. (2008). The thermal conductance of each die is obtained (19) to compute the longitudinal (two front dice minus two back dice) and transversal (two left dice minus two right dice) differential conductances: G_{long} and G_{trans}. These differential

conductances are both proportional to the Nusselt number and therefore related to the wind speed (Domínguez et al. 2008).

The calculation of the thermal conductance of each die requires the estimation of the convection power. To reach its thermal equilibrium, the power injected to each die has to equal the conduction and radiation power losses plus the power lost by convection to the ambient. These losses are estimated from the conduction and radiation constants obtained from a series of calibration tests (see Sect. 4.9.2).

$$G = \frac{P_{convec}}{T_{hot} - T_{air}} = \frac{P_{delivered} - P_{conductionloss} - P_{radiation}}{T_{hot} - T_{air}} = hA \tag{19}$$

$$h = Nu\frac{k}{L} = g(Re, Pr)\frac{k}{L} \tag{20}$$

where A is the dice surface, k is the CO_2 thermal conductivity, L is the characteristic die dimension, Pr is the Prandtl number of the fluid, and Re and Nu are the Reynolds and Nusselt numbers respectively for that fluid and speed. With the ambient temperature and pressure it is possible to compute the fluid properties establishing the relation between G and Re, and therefore between G and (U_∞, θ, ϕ). This is the reason why G_{long} and G_{trans} are used in this sensor as estimates of the local components of the wind speed at each recording point.

Boom Selection Algorithm As described in Sect. 4.1, to make the wind measurement more robust, two booms separated 120° are installed on the rover mast. This configuration assures that for most of the wind directions there will always be one boom outside the mast wake. To identify the best boom for the wind determination we prepared a look-up-table extracted from a set of CFD simulations run at representative "average" Gale conditions (700 Pa, 223 K, CO_2 atmosphere, two wind speed ranges (0–20 m/s and 0–70 m/s), and a range of different incident angles) using a simplified model of the rover, which includes the RSM mast where both booms are located. The local components at the location of all the thermal anemometers was registered, and a database with those local components and with the wind flow speed and yaw and pitch angles was produced. The look-up-table provides a series of rules which are applied to the two boards which give the highest readings for the local components for each boom. The rough estimate of the wind direction is based on sorting the local components, their signs, as well as sorting the two components ratios for each board. The rules were identified after analyzing the results of 90 simulations of the base set at constant speed (10 m/s), varying both the pitch and yaw angles. A fine tuning of the rules was necessary when all Reynolds numbers were considered (particularly for the lowest and the highest wind speeds). This algorithm gives an estimate of the wind horizontal direction (yaw) with a maximum precision of ±30° and a minimum precision of ±90°. For predicted direction intervals contained in [−90 90] boom 2 will be selected, and boom 1 for direction intervals contained in [90 270]. When the predicted direction isn't fully contained in either interval, it means both booms are receiving a strongly distorted flow, and boom 2 is selected, as it has proven to be more accurate in average than boom 1 in these circumstances (see Fig. 17) showing the booms' positions and their prediction intervals). This algorithm will be refined with real test data of two booms mounted on an RSM mast dummy in the linear tunnel facility at INTA.

Inverse Model Algorithm The wind speed retrieval method is based on querying a look-up-table obtained through extensive testing campaigns for a 3-D training mesh: pitch, yaw and Reynolds numbers (wind speed). The query is done for 4 local components of the selected boom (two boards with two local components each). The (pitch, yaw) pair, which minimizes

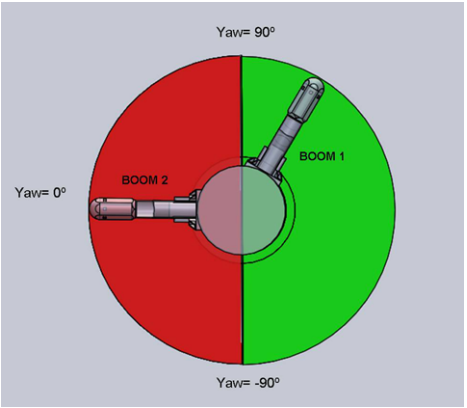

Fig. 17 Diagram showing the intervals for which each boom is selected as input for the inverse model. If the first iteration of the wind direction prediction is contained fully in either of these intervals, the selected boom will be the one indicated in the diagram. Boom 1 for interval [90 270] and boom 2 for interval [−90 90]

the difference in the local components is selected as center point for the interpolation of a finer grid mesh database with interpolated values for the two boards local components. The new interpolated database is again queried, retrieving as solution the mesh point (pitch, yaw, Reynolds) which minimizes the local components readings difference. Independent retrieval tests with training and non-training mesh data have been carried out and have shown that the initial pitch and yaw angle retrieval to be used as center for the finer mesh interpolation is achieved. This will guarantee the 30° error requirement, as the training mesh currently used is finer than that. The Reynolds number retrieval algorithm will require additional training data. Figure 18 shows the two components response for several tested Reynolds numbers, at yaw = 60° for pitch = 0°, as well as the longitudinal and transversal conductance response for several Reynolds numbers and yaw = 0° and pitch = 0°.

4.9 Wind Sensor Calibration

During the instrument development phase, the wind sensor's sensitivity to electrostatic discharge during frequent manipulation was readily realized, and therefore it was decided to avoid the risk of damaging the FM units and to perform the wind sensor calibration on wind tunnels with fully representative models called the REMS Calibration Models (CM) instead. For the WS tests to be representative we required: (1) same model geometry, (2) same materials and manufacturing processes and (3) same operation Reynolds and Prandtl number. The CM fulfills the first two and the third requires to reproduce gas composition, pressure, wind speed and temperatures. Three Mars facilities were considered, but some drawbacks were detected in all of them: the NASA AMES Mars wind tunnel is only operated with nitrogen; the new Mars tunnel at the University of Aarhus was not yet operative and Oxford University Mars tunnel test section proved to be too small for testing REMS wind sensor. Due to this, a facility was developed for the calibration of the REMS WS at CAB. At INTA Mars wind linear tunnel facility, full tests are being performed with the CM model and the same batch of tests compared with CFD simulations.

Due to the use of identical materials and manufacturing processes for the Calibration Models (CMs) and the Flight Models (FMs), both showed the same performance. Three types of tests were conducted on the FM and CM models: one set of minimally intrusive tests on both the FMs and the CMs to characterize electronically the models, a second set of tests (also done on the FMs and CMs) to determine in detail the possible manufacturing differences between them, and the third set of tests, more intrusive that are being done

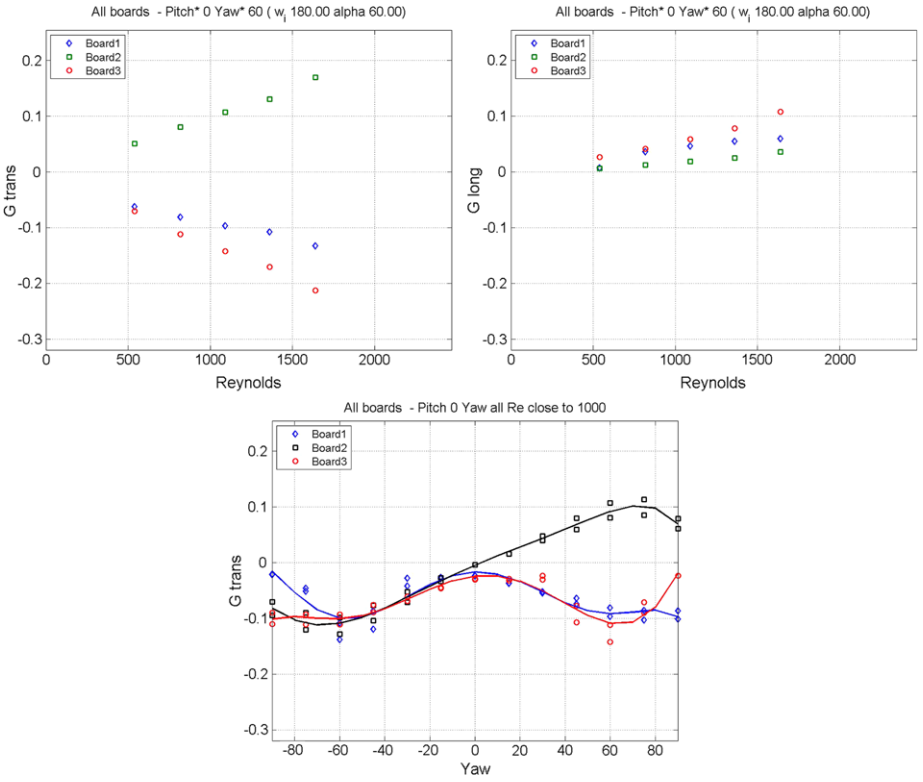

Fig. 18 Wind sensor calibration curves representing in the *first two figures* the longitudinal and transversal conductance versus several Reynolds number for pitch = 0° and yaw = 60°. In the *third figure* the transversal conductance is represented for all yaw angles at pitch = 0°

only on the CMs at the INTA linear wind calibration facility to determine in detail the aerodynamic response of the sensor, which is identical to the response of the FM as it only depends on the mechanical design of the sensor.

The electronic characterization of all models consists on the measurement of heater currents, polarization and reference currents, comparator offsets and amplifier gains for several voltages. It also includes the characterization of the resistivity of the platinum alloy of the dice. These variables are needed to calibrate the factors converting from measured voltages to the heating power needed to estimate the winds.

The calibration of the WS temperature sensors is performed following the same procedure as the PT1000s of REMS ATS, and is described in Sect. 4.3.

In order to optimize tests and simulations, the effect of temperature (in ambient, boards and hot dice) will be compensated, so that the same set of calibration tests and simulations (performed at a single temperature) are valid for the wind speed retrieval when operating under all circumstances. From the CFD simulations used to compare with the calibration tests it was determined that Nu can be computed as a product of a function of Re and Pr and another function of hot die and air temperatures (see (21)). The thermal effect compensation is being validated in a series of tests on the CM at several temperatures.

$$Nu_{compensated} = g_1(Re, Pr)g_2(T_{hot}, T_{fluid}) \tag{21}$$

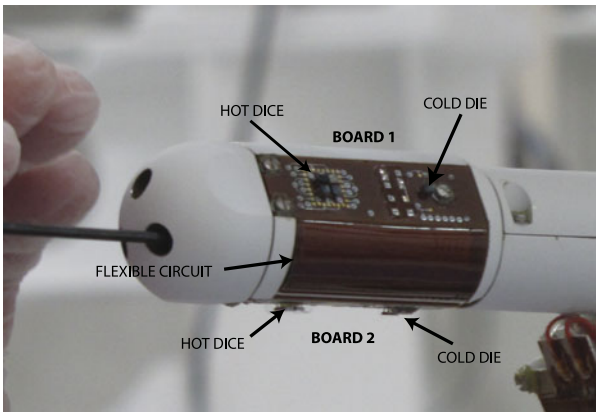

Fig. 19 Image taken during the REMS integration showing two of the WS boards. Each boom has three boards (Boards 1 and 3 in the sides, and 2 in the lower part of th boom) totally identical. Board 1 and 3 are connected to Board 2 by a flexible circuit and this is connected to the ASIC, in the back of the boom, by another flexible circuit. Each board has four hot dice and one cold die (the four hot dice are in the front of the board and the cold one is in the back). All dice are identical, manufactured in silicon, with three resistors printed on the upper side and thermally isolated from the board by four pillars with a low thermal conductance. In the hot dice, a resistor is used to heat it, another one is used as a sensor to measure the temperature, and the third one is used as reference sensor in the measurement circuit. In the cold die, the only resistor used is the reference resistor (for details see Domínguez et al. 2008). The control loop compares the temperature of the hot dice with that of the cold die, to control the power injected to keep a constant predefined temperature difference (delta temperature) between them. Each board has an additional thermistor on its inside face to monitor the board's temperature and evaluate the conductive thermal losses of the dice. (Credit: NASA/JPL-Caltech)

where Nu is the Nusselt number, Re the Reynolds number, Pr the Prandtl number, and T_{hot} and T_{fluid} are the temperatures of the hot dice and of the surrounding fluid respectively. Function g_2 will be validated in the thermal tests mentioned before.

The specific wind sensor calibration tests are listed below and described in detail in the following sections.

- Dice heat loss coefficient estimation. These tests are performed with FM and CM at vacuum from 180 K to 320 K.
- Boom local components calibration. These tests are done on calibration model at CO_2 and similar Reynolds to expected on Mars (pressure from 7 to 1013 mbar and temperature 298 K). These tests are also reproduced with simulations.
- Reduced RSM Mast and Boom local component calibration. Test on calibration models mounted on a section of cylinder reproducing the RSM mast, in CO_2 and similar Reynolds to expected on Mars (pressure from 7 to 1013 mbar and temperature 293 K approx.). These tests are also reproduced with simulations, in order to verify the correction factors to be applied to the local readings due to the mast perturbation as well as the boom selection algorithm.
- Simulation of the rover perturbation on the wind sensor. Simulations performed in EFD-Lab under Martian conditions to estimate the correction factors and to extract the decision rules for the non-wake boom selection algorithm.

4.9.1 CAB Mars Simulation Linear Tunnel Facility

It consists of a 500 mm diameter tunnel, six meters long, that moves the test bench at variable speeds under different ambient conditions (see Fig. 20). The test bench consists of a pan and tilt unit that can rotate the sample $\pm 90°$ in pitch and $\pm 180°$ in yaw. The following test conditions are able to be reproduced:

- Pressure: 1 mbar–1000 mbar
- Temperature: ambient
- Velocity: 0.05 m/s–1 m/s
- Tunnel Environment: Any gas

There are four pressure sensors that control the pressure in the chamber. Three were chosen due to their working range between 3 and 12 mbar (Mars pressure range), the fourth measures between 100 mbar and ambient. A DC motor & control moves the linear guide in a low friction constant velocity movement. The control box is linked to a computer application that enables the recording of all parameters such as temperature and pressure inside the tunnel and vary and record velocity and position of the test item in the linear guide. The aim of this tunnel is to calibrate the CMs of the REMS Wind Sensor and of the Air Temperature Sensor. Readings are recorded every second. Higher speed regimes are studied by modifying the Reynolds number. For an equivalent Reynolds number density and velocity can be varied.

$$Re = \frac{\rho V L}{\mu} \tag{22}$$

At equal temperature, fluid and tested item:

$$Re_1 = K P_1 V_1 \tag{23}$$

$$Re_1 = K P_1 V_1 = K P_2 V_2 = Re_2 \tag{24}$$

where Re_1 is the Reynolds number for a tested combination of pressure (P_1) and speed (V_1) and Re_2, another combination of pressure and speed, but in such a way that $Re_1 = Re_2$. K is a general constant, function of the fluid characteristics. The validity of the pressure/speed compensation through the Reynolds number has been verified for the wind sensor in the CAB Mars Simulation Linear Tunnel, the simplified Fig. 21 shows identical response of several wind sensor dice under three possible combinations of pressure and speed giving a unique Reynolds number

4.9.2 Dice Heat Loss Coefficients Estimation Test

This calibration test is performed on all models (flight and calibration). It is performed in a thermal vacuum chamber covering a wide temperature range. The test is designed to quantify manufacturing differences between the booms. As a result of physical differences of the models, each die on each wind sensor can have a particular conduction coefficient to the transducer board. It is necessary to measure these heat conduction coefficients to determine the heat loss from the hot dice to the transducer board. As a part of this test, the radiation coefficient of the hot dice is also obtained (in this case, the coefficient is the same for all dice).

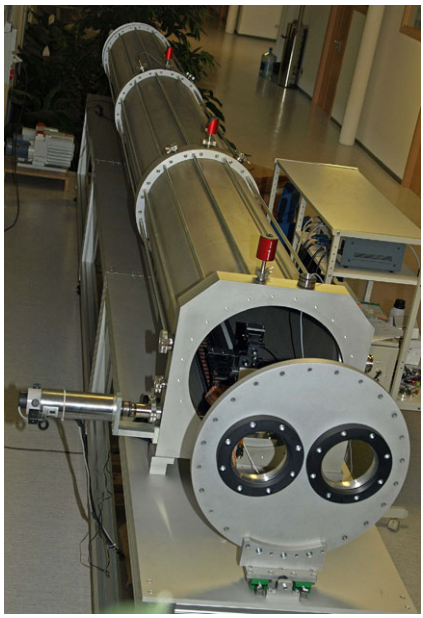

Fig. 20 Image of the Mars linear tunnel facility at CAB. *Inside*, a pan and tilt device allows to configure booms orientation

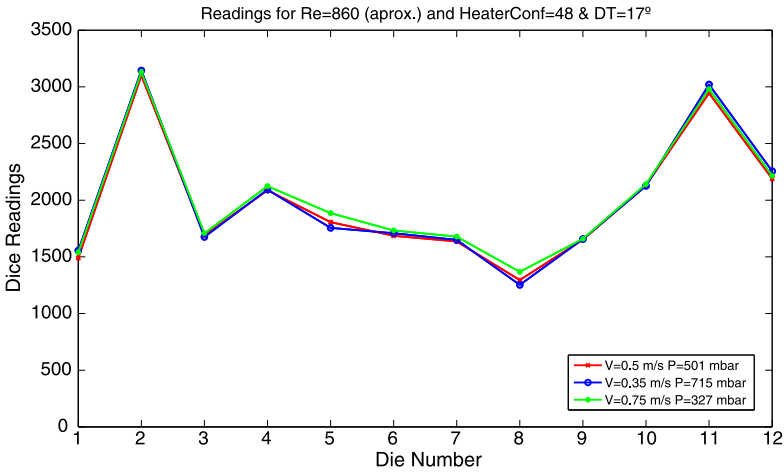

Fig. 21 Dice readings at identical Reynolds number, but with different combinations of pressure and speed. As the temperature of all tests is the same, the conduction and radiation losses are identical, and therefore the injected power to each die can be compared varying only pressure and speed. These results correspond to tests at Yaw = 0° and Pitch = 0°

The test was performed with several power configurations (Heater Currents) at several ambient temperatures. The power delivered for a die to reach thermal equilibrium is:

$$P_{delivered_i} = P_{conduction_i} + P_{convection_i} + P_{radiation_i} \tag{25}$$

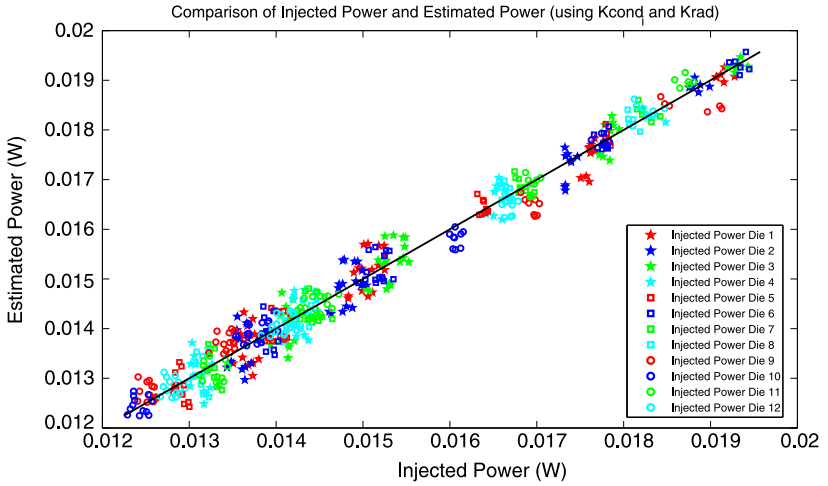

Fig. 22 Real injected power versus Estimated Injected Power for all dice. The identity line is represented in black to evaluate the dispersion between estimated and real power. The tests represented here reflect results in the range from −50 °C to +25 °C with several heater current configurations and voltages

As the tests are performed in vacuum, there were no convective power losses, and (25) will be simplified to (26), which is the general power equilibrium in a die.

$$\begin{aligned} P_{delivered_i} &= P_{conduction_i} + P_{radiation_i} \\ &= K_{cond_i}(T_{Hot_i} - T_{Board}) + K_{rad}\left(T_{Hot_i}^4 - T_{ambient}^4\right) \end{aligned} \tag{26}$$

Where K_{cond_i} is the conduction constant in die i and K_{rad} is the radiation constant.

For each tested case (heater configuration and temperature) on a boom with 12 dice, 12 equations such as (26) are obtained, in which the only non-determined parameters are K_{cond_i} with $i = 1 \ldots 12$ and K_{rad} common to all dice. The 13 parameters were obtained with a multiple regression over all sets of tested data. Figure 22 shows the comparison between the estimated injected power and real delivered power for all dice in the thermal vacuum tests of FM1.

4.9.3 Boom Local Components Calibration Test

The aim of these tests is to characterize the aerodynamic response of the wind sensors to different wind directions and wind speeds at Martian pressures. To that end, the tests were conducted at low density CO_2 atmosphere, room temperature, and performed in the range of Reynolds numbers expected on Mars. The wind direction and speeds testing mesh used is:

- Pitch: −90° to +90°
- Yaw: −150° to +150°
- Equivalent Speed: 0, 1, 2.5, 3.75, 5, 7.5, 10, 12.5, 15, 20, 30, 40, 50, 60, 70 m/s

The injected power is calculated for each test using the readings of the wind sensor as well as the board and ambient temperatures. Applying the conduction and radiation coefficients it is possible to obtain first the convective power of the dice, and also the convective

thermal conductance to the ambient, G, as described previously. Finally the "Longitudinal Conductance" and the "Transversal Conductance" are also calculated for each board as shown in Fig. 18. The results of these tests are the input for the inverse model training database. The same tests under identical conditions are simulated in EFDLab Program. With the results from both, real tests are identified with the thermal and aerodynamic EFDLab simulations.

4.9.4 Reduced RSM Mast and Boom Local Components Calibration Test

Similarly to the Boom Local Components Calibration Test, a set of tests with two calibration booms mounted on a cylinder representing the Rover Mast will be subject to several speeds and directions at INTA Mars Simulation Linear Tunnel facility. A set of simulations identical to the wind tunnel tests are being done to verify the validity of the simulated model. In this way, the boom selection algorithm obtained from the full rover simulations is verified and fine-tuned with real data.

4.9.5 Simulation of the Rover Perturbation on the Wind Sensor

The rover perturbation on the wind sensor is simulated with EFDLab in order to determine the correction factor to be applied to the wind speed calculated with the perturbed readings of the wind sensor. This set of simulations covers the complete possible mesh of wind speeds and incident angles (both horizontal, yaw, and vertical, pitch). The wind speed measurement needs to be corrected as a consequence of the RSM mast and rover perturbations if one wants to estimate the background wind in absence of the Rover influence. This correction is based on CFD simulations because an aerodynamic rover scale test is not feasible with the actual facilities. Two sets of CFD simulations are compared to introduce a wind speed correction factor accounting for the rover perturbation: (1) Simulations with only the boom, (2) Simulations including the rover and the boom mast. For each yaw and pitch of the test mesh, the wind speed correction curve for the non-calibrated rover presence is calculated: The wind flow speed at 3 boom diameters distance is compared in both simulations for several free flow speeds. This correction factor will use the rover perturbed wind speed measured at the booms to estimate the unperturbed free flow speed. This effort will remain active during the mission as we learn from the results, but at the start it will be assumed that the correction factor is constant for yaw $\pm 15^\circ$ and for pitch $\pm 15^\circ$ so as to avoid additional interpolation complexity.

4.10 Ultraviolet Sensor

The REMS-UV sensor measuring concept is based on the use of 6 UV photodiodes, provided by Ifw Optronics GmbH, of different spectral support. UV photodiodes have the advantage of being small in size, light and robust for survival and operation under harsh conditions such as those expected for MSL. The REMS-UV sensor is placed on the rover deck, facing the sky, at a location that is visible by the rover Navcam. Each photodiode weights 1 g and consists of a TO-5 housing (of 5 mm height and 5 mm diameter) with a SiC sensing surface of 1 mm^2 and a nominal field of view (FOV) of $\pm 30^\circ$. The FOV is geometrically limited by the photodiode caging. When the Sun is within $\pm 30^\circ$ with respect to the norm, the direct beam reaches the sensing dice directly or after traverse of the filter (if any). Each photodiode is embedded in a samarium cobalt magnetic ring to deflect the trajectories of in-falling dust and mitigate dust deposition. An additional magnet is placed in the center of the box below

a white area. This area shall be used to evaluate during the mission, using camera images, the sensor degradation due to dust deposition.

The selected photodiodes have different spectral ranges: one global (named ABC) SiC photodiode with responsivity in the range 200–380 nm, and 5 filtered photodiodes named A, B, C, D and E. Each broadband photodiode shall provide an approximate evaluation of the incident flux within its range of responsivity: photodiode C provides a first order estimate of the level of biologically damaging irradiance; the outputs of photodiodes A and B are to be compared with terrestrial irradiance while photodiode ABC gives an estimate of the total UV irradiance, and photodiodes D and E are designed to match two UV channels of the MARCI instrument on board the Mars Reconnaissance Orbiter (MRO) satellite such that a direct comparison with simultaneous reflectance measurements is possible. Each individual photodiode provides information that can be directly compared with their equivalent measurements on Earth or on the top of the Martian atmosphere. But besides, the combined use of the simultaneous measurements of the 6 photodiodes will provide not only better estimates of the incident irradiance per channel, but also a smooth approximation to the spectral shape of the down-welling flux.

Transfer Process To obtain the band integrated irradiance per channel, the usual approach with narrowband radiometers is to calibrate the responsivity. This factor is usually called responsivity R by the manufacturer and is associated with an average (or weighted average) of the spectral responsivity of the photodiode. This scalar factor relates the output of the sensor (a current) with the incident band integrated irradiance. The scalar factor approximation is fairly good provided that the spectral range of the radiometer is narrow, that the spectral shape of the irradiance within the spectral support of the detector is smooth or that the response is calibrated for a known spectrum, where only the intensity level is expected to change and the spectral shape is constant. However for intermediate to broadband sensors, as it will be illustrated later on, this scalar factor is dependent upon the spectral shape of the incident irradiance.

For REMS UV in-situ measurements the challenge is to deliver integrated flux values per channel for varying, unknown, spectral shapes of the incident UV irradiance. The down-welling irradiance depends on the total mass of dust and ozone which in turn may change strongly from one acquisition to another (because of the variation with Solar Zenithal Angle of the path traversed) and also along seasons (due to atmospheric chemistry processes and to the natural dust cycle evolution). Since the dust scattering processes are non-linear, an increment in the total column of dust seen by UV photons will lead to a change in the spectral shape of the diffuse irradiance and, if ozone traces are present, the ozone absorption band will be enhanced in the diffuse component of the irradiance (Zorzano and Córdoba-Jabonero 2007; Zorzano et al. 2009). Furthermore the spectral irradiance exciting the photodiodes may also change abruptly with the sudden passage of dust devils or clouds within the line of sight of the direct beam coming from the Sun.

The response of the photodiodes under different experimental environments has been investigated, the responsivities are summarized in Table 6. The setups considered the response to a Deuterium lamp (D_2) in vacuum (V), response to a Deuterium lamp in ambient conditions (A, and thus with ozone absorption), response to a collimated Xe lamp and response to a distant Solar emulator Xe lamp within the end-to-end STT REMS tests in N_2 ambient with the MSL rover completely integrated. For comparison the averaged response of the photodiodes, as provided by the manufacturer, is shown. This illustrates the dependence of the responsivity with the spectral shape of the irradiance. For each scenario, the incident band-integrated flux can be retrieved by dividing the output current of the sensor by the corresponding factor R in Table 6.

Table 6 Responsivity R of each channel at 25 °C and normal incidence, for different incident spectra (Deuterium lamp D_2 under ambient A or vacuum conditions V, xenon Xe collimated and in the STT integrated tests) and averaged spectral response

Scalar responsivity [nA/(mW/mm^2)]	$R^V_{D_2}$	$R^A_{D_2}$	R^{Col}_{Xe}	R^{STT}_{Xe}	$R_{Averaged}$
ABC	0.101	0.095	0.074	0.081	0.096
A	0.044	0.045	0.037	0.034	0.038
B	0.147	0.135	0.142	0.139	0.142
C	0.083	0.060	0.129	0.116	0.098
D	0.035	0.024	0.043	0.040	0.038
E	0.054	0.057	0.060	0.571	0.06

Notice that for narrow band channels such as B and E the scalar factor R is, to first order, similar across all the scenarios and thus practically independent of the spectral shape of the considered incident irradiance. Photodiodes C and D are sensitive to the ozone absorption band and thus the spectral shape in this area changes strongly from one scenario to other. As for the ABC and A photodiodes the bandwidth is relatively big and the responsivity depends strongly on the shape of the spectral irradiance. As expected, the R factor varies with the spectral shape of the responsivity (and thus with temperature and angle of incidence) but mostly, as illustrated above, with the spectral shape of the incident radiation. Through these examples we have illustrated that for an arbitrary incident spectral shape the power cannot be correlated with the current of the photodiode by simply applying a universal scalar factor.

To cope with this, an specific algorithm has been developed to retrieve from the 6 broadband measurements of REMS filtered SiC photodiodes an added value product: a smooth approximation to the incident spectrum. This is possible due to spectral support of the chosen photodiodes, which have intersecting ranges of spectral responsivity. In other words, this retrieval process transforms REMS-UV photodiode sensor into something intermediate between a radiometer and a spectro radiometer. This mathematical method, whose details are described elsewhere (Vázquez et al. 2007; Zorzano et al. 2009), has been validated numerically. The accuracy of the retrieval model alone can be as good as 0.6 % or better within each channel for smooth spectra.

As an example of application for Mars we next provide some extreme scenario of REMS outputs, and deliverables for a clear scenario with the direct beam of the Sun at normal incidence when the atmospheric opacity is given by $\tau(\lambda\ [\text{nm}]) = 0.782\frac{210}{\lambda^\alpha}$ with Angstrom exponent $\alpha = 1.1$ which corresponds to a visible optical depth of $\tau(650\ \text{nm}) = 0.23$, at an equatorial location, during perihelion and assuming a temperature of 25° within the rover deck. For this hypothetical case the modeled incident spectra is convoluted with the spectral responsivity and the output delivered currents are evaluated. Using the currents and the responsivities as an input for the retrieval mathematical process an smooth approximation is obtained, see Fig. 23. The integral UV flux for each channel is then calculated and compared between the initial incident modeled spectrum and the output of the retrieval. The results are summarized in Table 7. For comparison the corresponding R parameter is shown. As above, the parameter R is the scalar factor that relates the output current with the incident integrated irradiance for this spectral shape. The accuracy column indicates the difference between the UV flux per channel obtained from REMS(fit) and the one obtained knowing the incident spectrum line by line. The accuracy errors are mostly due to the difference between the smoothly varying fit and the line to line variation of a solar spectrum. The retrieved

Table 7 Example of REMS deliverables for a plausible Martian scenario: current induced by a direct equatorial UV irradiance at perihelion, and normal incidence, assuming optical depth of 0.23 at 650 nm and Angstrom exponent $\alpha = 1.1$ and sensor temperature 25° (within the warm part of the rover deck)

Channel	Wavelength range [nm]	I [nA]	R [nA/(mW/mm^2)]	F_{fit} [W/m^2]	$F_{Spectrum}$ [W/m^2]	Accuracy [%]
ABC	200–380	1842	0.0663	27.8	29.9	7
A	320–380	646	0.036	18	18.9	5
B	280–320	651	0.134	4.85	4.71	3
C	200–280	140	0.106	1.31	1.38	5
D	230–290	73.8	0.0374	1.97	1.81	9
E	300–350	692	0.0592	11.7	12.8	2

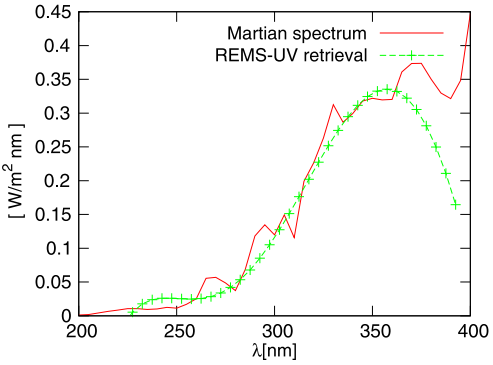

Fig. 23 Example of REMS based fit of the incident spectrum for an hypothetical scenario of UV measurements on the Martian surface, details above. (Credit: CAB (CSIC-INTA))

spectrum is valid within the interval 220–370 nm which is the area where the photodiodes have spectral sensitivity.

It is remarkable that the scalar responsivity factors for the Martian-like spectra are comparable within 10 % with the Xe responsivities for channels ABC and B, and within 1 % for channels A and E. However for channels C and D (those dedicated to ozone absorption), the variation goes beyond 15 %, since the shape of the Martian solar UV irradiance differs widely in this range from the one of the Xe lamp. In summary, the scalar responsivity values shown above can be used for quick look calculations, but during operation the full retrieval algorithm shall be applied to the set of 6 currents to retrieve a smooth approximation to the spectral shape of the incident irradiance and from here the integrated irradiance within each wavelength. By doing this we avoid the error associated with variations in the spectral shape of the irradiance.

Applying this specific processing to REMS-UV deliverables (currents), and taking into account the calibrated spectral responsivities (at a given temperature and corrected by the angle dependent factor), the retrieval process delivers an smooth approximation to the UV spectral irradiance together with REMS-UV nominal deliverables, namely, the band-integrated flux per channel. The smooth approximation of the UV spectrum provided as by-product of the retrieval process, is extremely interesting and shall be used to provide more insight into scientifically relevant issues such as: (1) evaluation of specific biological damaging doses (DNA, protein, skin doses, etc.), photolysis rates and oxidant production (to asses the habitability of the Martian surface), (2) daily evolution of the spectral opacity (to monitor atmospheric dust load, size and absorption-scattering properties), (3) seasonal variation

of the absorption band of ozone which serves as proxy for water vapor and (4) comparison with radiative transfer models and satellite measurements (Zorzano and Córdoba-Jabonero 2007).

The functional requirements of the REMS-UV sensor were specified for a non dust-degraded sensor. The main plausible limitation for this sensor is its degradation due to dust deposition within the line of sight. A mitigation strategy has been implemented, using magnetic rings to deflect the trajectories of infalling dust and camera images to calibrate the obscuration of a white control target. Further error sources are associated with the contribution of the unfiltered diffuse irradiance in particular to those channels where the signal is expect to be small (namely C and D) (Zorzano et al. 2011), the approximation of the incident spectrum by a smooth function (as shown above) and the errors in the calculation of the solar incidence angle of the direct beam at the time of acquisition. Finally also the electronic errors have been taken into account. The original functional requirements of REMS photodiodes were to deliver integral UV irradiance measurements with a resolution better than 0.5 % and accuracy better than 10 % with respect to the maximum expected values. These values were given because of expected instrumental capabilities. However, in practice, and according to the laboratory and field site validation of the instrument, the accuracy is expected to be of the order of 5 % (or even better) w.r.t. acquired value.

4.11 Ultraviolet Sensor Calibration

The values of the spectral response at different temperatures and angles of incidence are needed to retrieve from the output current the corresponding incident UV flux. This information is obtained in the calibration process. The response of the flight model and spare photodiodes was calibrated at ALTER Technology Group (Spain) in a nitrogen N_2 chamber with a UV transparent window. The N_2 atmosphere creates a neutral environment (to avoid the ozone molecular absorption of terrestrial air). The calibration setup consist of a Deuterium (D_2) lamp as UV source (Hamamatsu L2D2), an optical bench, focusing optics, a monochromator, a beam splitter and a multimeter. For traceability of the calibration process, the response of three photodiodes under different conditions was characterized at the National Physics Laboratory (NPL, UK) calibration laboratory, for spectral response (ABC type, reference report E07060366/1), linearity (B type, reference report E07060366/2) and angle dependence (E type, reference report E07060366/3). The REMS-UV calibration setup was referenced with these results. All the calibration measurements were performed after a long warm-up period of the UV lamp (of the order of 4500 s), as it was observed that this time is required to achieve full stabilization of the UV spectral profile and intensity. The following list summarizes the main calibration studies.

- Spectral scanning, absolute calibration. Test to retrieve the spectral responsivity of each photodiode type at normal incidence (and compare with specifications), carried out in a nitrogen atmosphere and ambient temperature.
- Spectral scanning, absolute calibration. Similar to previous one but in temperature range from 138 K to 373 K.
- Linearity calibration at varying temperature. To confirm linearity of response at normal incidence and varying operating temperatures. Test conditions were: Nitrogen atmosphere, 138 K to 373 K. During the tests some filters were used to varying opacity to reduce incident signal.
- Spectral scanning, angle dependence. To retrieve the spectral responsivity of each photodiode type for varying angles of incidence of the direct beam. Tests conditions: nitrogen atmosphere and ambient temperature.

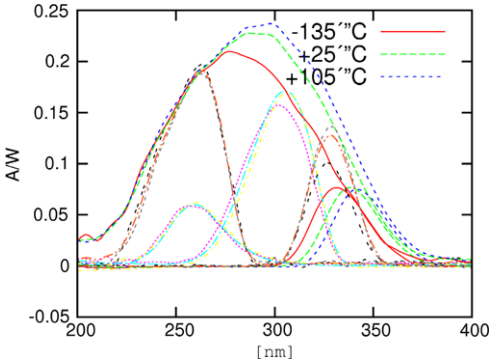

Fig. 24 Temperature dependence shift of the SiC responsivity (channel ABC) and influence on the spectral responsivity of channels A, E and B. (Credit: CAB (CSIC-INTA))

– Internal temperature sensor calibration. To calibrate the sensor response that is used to determine the operating temperature of the UV box in a nitrogen atmosphere and varying the temperature from 138 K to 373 K.

As an example, next we show some of the products of the calibration in temperature for the spectral responsivity. The SiC UV quantum efficiency, varies slightly with temperature specially for higher wavelengths (lower energy photons). The filter spectral response may change with temperature as well. The UV box is embedded within the warm part of the rover and therefore the sensor temperature is expected to vary slowly and within a much narrower temperature range that the nominal calibration temperature interval. This temperature will be continuously monitored by the RTD sensor of the REMS-UV box. Within this thermal range and for wavelengths longer than 280 nm, the responsivity of the SiC dice increases with temperature (about 1 % per °C) and shifts (about 10 to 20 nm) towards longer wavelengths, see Fig. 24 for an illustration of this spectral change in the responsivity. This effect is the dominant one, and thus photodiodes whose spectral response are sensitive in this area, namely E, A and partly B, show a significant temperature dependence. This effect shall be taken into account in the retrieval model using the spectral responsivity of the corresponding temperature in the transfer process.

The spectral responsivity curves within [200–400] nm, equivalent to the ones shown above at normal incidence, have been obtained for varying angles of inclination at ambient temperature. It has been observed that the response does not decay as cosine law but as a $\cos^a$-law instead (with $a = 5.765$ from NPL data fit and in agreement with the observed angle dependence of the spectral calibration).

Linearity of the response is essential to assume that the calibration products, obtained at a given incident spectral power, can be extrapolated to arbitrary irradiance levels on Mars. According to the manufacturer the linearity of the photodiodes is of the order of 1 %. This has been verified within the range [0.12–0.5] W/m^2 at NPL for a B type photodiode. Finally this has been calibrated for all photodiodes types, using the N_2 temperature chamber, at different temperatures. The UV lamp was operated at maximal power. To reduce the incident power a set of UV filters with different opacities were placed in the beam path and the total, integrated power of the lamp plus filter was recorded at one end of the beam splitter.

In summary, the overall spectral responsivity of the photodiodes for a given angle of incidence (θ) of the direct Sun beam and a known temperature of the UVS box, is obtained by interpolation of the calibrated responsivities at fixed temperatures to the desired temperature point and correction by the $\cos^a(\theta)$ factor with θ the solar angle of incidence to the photodiodes (i.e. taking into account the rover tilt at the moment of acquisition). In fact this later

correction factor by a scalar factor may be implemented on a second correction stage, once that is known the exact angle of the sun with respect to the photodiodes (this depends on the Sun position in the sky and on the rover tilt with respect to the surface at the acquisition time).

Additionally, a set of field validations have been performed to quantify the unfiltered contribution of diffuse radiation (Zorzano et al. 2011). The details of the calibration products are not within the goals of this paper.

4.12 Sensor Front-End ASIC

The sensor front-end is implemented by means of an ASIC. There is one of these devices on each boom. These devices are custom integrated circuits that receive all the low level analog signals generated on the sensors, and convert them into digital signals, which are transmitted to the ICU where the scientific data can be processed and stored.

Among other features, each front-end ASIC includes constant current sources that drive currents through all Pt1000 sensors (air temperature and ground temperature sensors) and measure the voltage drops and convert them into digital values; amplifies and digitizes the currents from the GTS thermopiles; and generates the currents for the 12 hot dice on the wind sensor, and convert the signals from the electro-thermal sigma-delta control loops into counts.

The ICU controls the operating temperature of each front-end ASIC by means of a heater and a thermistor bonded to each casing. It is based on a two-level strategy:

1. The heater is powered on when thermistor readings are lower than −55 °C, with an hysteresis loop of 5 °C ([−55, −50] °C).
2. The ASIC is powered on when its temperature is higher than −70 °C, becoming operative from −52 °C.

4.13 Instrument Control Unit

REMS has its own Instrument Control Unit (ICU) for monitoring and controlling all its sensors, and interfacing to the Rover by managing commands and telemetries. It is accommodated inside the Rover body, where the electronics equipment is kept at controlled and more comfortable temperatures by the Rover thermal control system. Its main functions are:

- Power conditioning for ICU and sensors.
- System initialization and self-testing.
- Communications (telecommand/telemetry) and interfacing to the Rover.
- Real time clock, alarm-counter and on-board time management.
- Operation modes management.
- Instrument timeline execution and data logging based on pre-programmed “schedule tables”.
- Sensors conditioning and/or interfacing; sensors control and data acquisition.
- Scientific data storage in non-volatile memory.
- Download of scientific and housekeeping data.
- Accommodation for the Pressure Sensor.

REMS instrument interfaces electrically with the Rover by means of only one physical connector of the ICU. This interface includes the power bus input (not redundant), an asynchronous serial line communication with redundant electrical interfaces, redundant discrete status lines and one not-redundant Platinum Resistance Thermometer (PRT) sensing interface.

The ICU is physically composed of three modules:

- A general-purpose Central Processing Unit (CPU) based on a standard 80C32E microcontroller (a radiation-tolerant version of the Intel 80C32 8-bit processor, by Atmel).
  The CPU implements a 32KB ROM for boot code storage and a 64KB RAM for data management. A 128KB EEPROM bank houses the application software and a 4MB non-volatile memory (flash memory) allows storing the scientific data temporally until they can be transmitted to the Rover.
  The CPU also includes a FPGA for supporting the low-level hardware logic and implementing the specific interfaces to the humidity and pressure sensors, and standard serial interfaces for communications with the Booms.
- A Power Supply Unit (PSU), which receives the main power bus from the Rover and provides conditioned secondary voltages as necessary for the operation of the REMS electronics. It includes two commercial high-reliability DC/DC converters and one custom small converter for powering the instrument alarm-counter during the sleeping periods (the so-called Stand-by converter).
  The PSU also guarantees the existence of a reliable power supply by implementing several protections, such as current limitation at primary side (Latching Current Limiter), current limitation and/or thermal protection at secondary side, electronic soft start, undervoltage protection at primary side and overvoltage protection of the +5 volts secondary output.
- An Analog/digital front-end Module (AM) to acquire and digitize the low level signals from the ultraviolet sensor photodiodes, some external temperatures and other internal housekeeping signals. It also implements the two thermal control loops in charge of warming-up the ASICs at the Booms, as mentioned, as well as the logic to control the pressure sensor On/Off powering and the humidity sensors heaters.

The REMS Pressure Sensor is also accommodated inside this ICU, although it is not considered a functional part of the ICU itself.

Table 8 summarizes the parameter used to sense the corresponding magnitude from each sensor, as well as the processes to sample and digitize those prior to be transmitted to ground.

In order to control all the functions above and hardware elements, the ICU includes two SW products: a Bootstrap basic SW (burned in PROM and non-modifiable) and an Application SW (in EEPROM), which can be modified during the mission and implements the REMS operation modes and the communication protocols. REMS software supposes around 8500 source lines of code written mainly in C language with a minimum assembler support.

As detailed in Sect. 5, this ICU's hardware and software architecture enables REMS to work autonomously, independently of the Rover compute elements.

Mechanically, the ICU box is assembled as a stack formed by three modules, as shown in Fig. 25:

- First Level (bottom) composed of the Analog Module and the Pressure Sensor. The stiffener of this module includes the mounting feet and serves as baseplate in contact with the Rover platform.
- Second Level (mid) is the CPU Module.
- Third level (on top) is the DC/DC Module.

The ICU is screwed headed-down to the upper interior part of the rover Warm Electronics Bay (WEB) deck Payload Mounting Panel (PMP). The Pressure sensor uses a small tube to interface with the Martian atmosphere (the tube passes through the ICU analog stiffener to a cavity in the PMP interior that is in turn open in its superior part to interface with the ambient atmosphere through a HEPA filter, and covered with a dust protection cap).

Table 8 Acquisition chain for each sensor

REMS sensor and abbreviation	Sensor output	Acquisition	Transmitted data type to ground
Air temperature (ATS)	Voltage drop	Front End ASIC includes pulsed constant current sources that drive current through the Pt1000 sensors.	Voltage drop digital value (counts)
Ground temperature (GTS)	Voltage drop (thermistor) Current (Thermopiles)	Front End ASIC differential programmable gain amplifiers (PGA). Low offset based on chopped switch capacitor technology.	Voltages and currents digital values (counts)
Pressure (PS)	Capacitance	Pressure ASIC multiplexer is used to multiplex sensors and capacitors as a capacitance onto a RC-oscillator. Frequency of the oscillator is measured	Frequency digital values (counts)
Humidity (HS)	Capacitance	Same as PS	Same as PS
Wind (WS)	Power injected into dice	Front End ASIC individual electro-thermal sigma-delta control loop supplies power to each hot die	Power supplied to each die is directly proportional to the counts provided by the sigma-delta converter
Ultraviolet (UVS)	Voltage	Transconductance amplifier inside ICU measures the current generated by the photodiodes. ICU analog front-end includes resistive divider using the Pt1000	Voltage drop

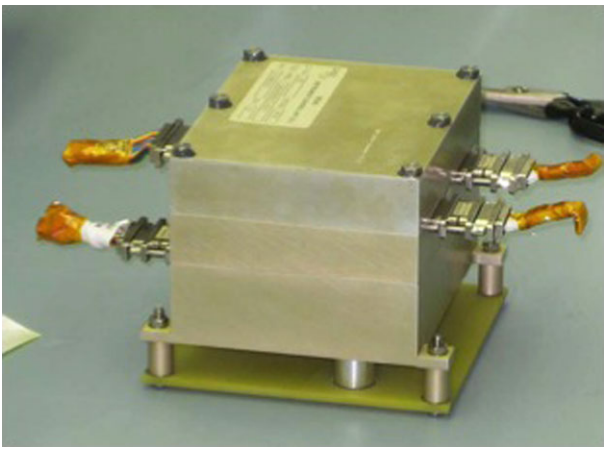

Fig. 25 ICU ProtoFlight Model during Bench Acceptance test at JPL. (Credits: CRISA)

Two complex (composed of several round and flat sections) bundles of cables running through the Rover Main Mast are used to interconnect the Booms with the ICU down into the Rover‘s deck. The UV Sensor mounted atop the surface of the Rover‘s deck is connected to the ICU by means of another cable bundle.

4.14 Instrument Performances

This section summarizes the REMS performances with the aim of making a possible comparison with precedent meteorological stations on Mars, shown in Table 1. Wind sensor data will be published once that the calibration tests were finished.

Pressure Sensor The sensor has been calibrated for Martian pressure range of 4–12 hPa (actually from vacuum to 14 hPa, see calibration section for details) and operational temperature of -45 °C…$+55$ °C. The resolution of the sensor (high-resolution sensor heads) is measured to be 0.2 Pa with the response time of the overall pressure measurement system being approximately 1 s. The stability of the high-stability sensor head during the surface operations phase is estimated to be <1 Pa/year. The absolute accuracy of high-stability sensor head is estimated to be 3.5 Pa root-mean-square after the first few weeks after landing.

Humidity Sensor The Humidity sensor has been calibrated to measure from 0 to 100 % RH and can survive even -135 °C ambient temperature, but below -70 °C the dynamic range of the Humicap® becomes too small for practical humidity observations.

Typical accuracy that can be achieved with REMS Humidity sensor is ± 2 % RH in 0 °C, ± 4 % RH in -40 °C, ± 8 % RH in -70 °C. The Humidity sensor reference model has been measured in several campaigns since delivery of the flight and spare models, and after regeneration of the Humicap® heads by heating, the sensor has achieved the same accuracy as right after the calibration campaign.

Ultraviolet Sensor After calibration the measurement range is the following one:

- Total dose: 200–370 nm (56.9 W/m^2)
- UVB: 280–320 nm (9.5 W/m^2)
- UVA: 315–370 (320–370) nm (25 44.2 W/m^2)
- UVE: 300–350 nm (10.6 W/m^2)

The resolution will be better than 0.5 % and the accuracy better than 5 % in output current.

Ground Temperature Sensor The GTS will measure the ground brightness temperature over the range of 150 to 300 K with a resolution of 2 K by averaging 1 minute reading. Sensor accuracy is better than 10 K, using only the 8–14 μm thermopile, whilst the ASIC temperature is above $-50°$.

Air Temperature Sensor The ATS will measure the air temperature near the booms over the range of 150 to 300 K, with a resolution better than 0.1 K and an accuracy better than 5 K, with the Wind Sensor switched off.

5 Instrument Operations

5.1 REMS Software Capabilities

From the software perspective, REMS instrument has been designed to operate either autonomously on the basis of a sequence of commands that are uploaded and stored into the instrument memory, or by means of dedicated instrument commands sent by the Rover computer.

When running autonomously, REMS instrument operates from a low-power sleep mode, which can be powered even while the Rover main compute element (RCE) is off. An internal timer wakes REMS to take observations according to the pre-determined schedule, saves the data internally, and goes back to sleep. The instrument housekeeping tasks can also be performed according to a schedule. The file loaded into REMS to control all these activities and the times when these are executed is known as Schedule Table (ST).

In case of being commanded directly by the RCE, the REMS instrument will execute the instrument commands at the moment they are received.

Basically, REMS is capable of performing the same set of activities in either (of the aforementioned) operational modes. However, the flexibility of the autonomous mode will allow REMS to take observations over night, when the RCE is off. This aspect is a critical factor in achieving REMS science objectives.

Besides these two working modes, the instrument capabilities are defined on the basis of a *Command/Telemetry Dictionary* that states the communication to/from the instrument. This communication between REMS and RCE is based on a command-response protocol where the RCE is always the master, and the instrument the slave.

The instrument Command Dictionary allows the RCE and, therefore, the instrument operators through it:

- Synchronizing and managing the instrument clock.
- Managing the built-in self test that the instrument performs during booting process.
- Managing the transitions between instrument states.
- Managing what copy (image) of the APSW is executed.
- Commanding REMS to load and enable/disable the execution of the internal Schedule Table.
- Managing the REMS EEPROM, RAM and Flash memory banks.
- Setting the internal configuration parameters that govern the instrument functionality.
- Performing sensor maintenance operations.
- Retrieving the scientific and engineering data recorded in memory.

Subsequently to those instrument commands, REMS generates and send a reply on the basis of the defined Telemetry Dictionary. Besides sending back the reports and engineering/scientific data to the Rover, the RCE is kept informed about the status of the instrument by means of these telemetries.

5.2 REMS Measurement Strategy

In order to attain the goal of performing long-term investigations of meteorological phenomena and the UV radiative environment REMS will regularly make brief measurements throughout the Martian day and night, over the lifetime of the mission.

Typically, REMS will be performing regular observations for approximately 5 minutes every hour, every day. Additionally to this baseline hourly observation cadence, the instrument will operate 60 minutes per sol in some special modes to take additional data. These special modes are: (a) scheduling additional pre-defined observation periods to examine phenomena of known interest, not exceeding those 60 minutes per sol; and/or (b) making real time comparisons between data taken during the hourly 5 minutes periods and a set of pre-defined values in order to algorithmically trigger additional observations immediately following the schedule hourly periods. This last case, namely, the *Event Mode*, tries to detect any ongoing episodic and transitory atmospheric event.

In addition to their value in understanding Martian meteorology, REMS results will be used to help understand the environment in which the other instruments and the rover are performing their tasks.

5.3 REMS Scientific Operation

Although REMS operation is mainly autonomous, a minimum communication between the instrument and the scientists/engineers on the Earth is required every sol. This communication provides the common framework for exchanging Instrument Commands and Instrument Telemetry between these two ends, using the RCE on the vehicle as relay.

The scientific operation of the instrument is based on the definition of a sequence of high-level *activities*, which are the essential building blocks of the surface mission, providing a structure for planning of science operations, as well as modeling of those operations. These activities will be the outcome of scientific daily meetings where data from previous sols are analyzed and commented, and will constitute the sequence of actions that all the instruments on the Rover (not only REMS) will execute in the coming sol. This one-sol turnaround commanding and execution cycle is called *Tactical decision procedure*, in opposition to the *Strategic decision procedure*, which is focused on the definition of long term scientific objectives and global resources allocation.

Participation of REMS team members on those tactical and strategic discussion and decision forums is stated on the basis of the roles defined by the MSL operation framework

It is also worth to mention that the tactical and strategic operation of REMS will not only fulfill the scientific objectives stated by the MSL Atmosphere and Environment Theme Group. Information provided by REMS will be of a valuable interest in contextualizing the science by the other Science Theme Groups (Volatiles and Isotope Geochemistry; Inorganic Chemistry and Mineralogy; Geology; and Atmosphere and Environment), as well as contributing to the generated cooperative science framework. As an example, the REMS wind forecasts will be decisive in order to schedule science activities which can only be performed under light winds, such as drilling, brushing collection and handling of regolith samples and their deposition in the SAM and CheMin inlet tubes on the rover deck.

5.4 Software Tools in Support of REMS Operations

In order to successfully fulfill their corresponding role objectives and the global MSL goals, REMS scientists and engineers involved in operations will make use of the Ground Data System (GDS). This GDS is made up of various software tools in support of their activities: data validation, processing and archiving, science analysis and instrument commanding.

The two main cornerstones within the GDS are: (a) MSLICE, a software tool developed by JPL in charge of general science surface operation visualization, activity planning, resource modeling and allocating, and commands sequencing; and (b) QRS, developed by the REMS team and specially focused on the REMS-specific data visualization and analysis, instrument health assessment, and generation and validation of the ST prior to be transmitted to Mars. Figure 26 shows a snapshot of QRS being used to analyze the air temperature data flow.

The precise concatenation and engagement of all these elements (scientists, engineers, tactical and strategic meetings, ground software tools, instrument flight software) guarantee an optimal operation and resources utilization, and maximize the science return from Mars.

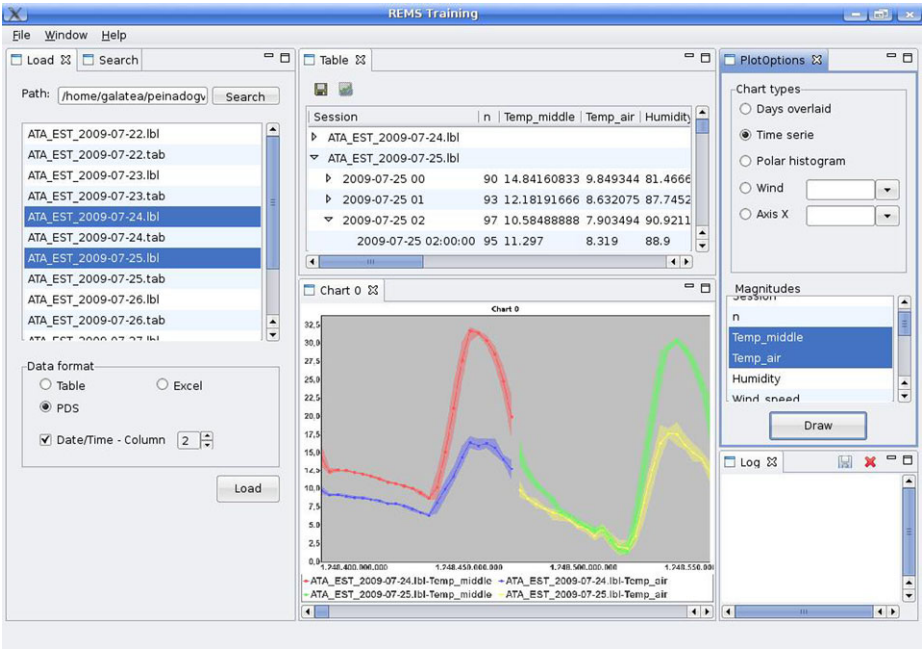

Fig. 26 REMS QRS multiplatform tool

5.5 REMS data for the Planetary Data System

In consonance with MSL project and NASA directives, on-ground REMS data products will be generated, validated, transferred and archived according to the Planetary Data System (PDS) regulations. REMS is assigned to the *PDS Atmospheres Node*.

Binary raw data products from Mars (mainly, instrument telemetries with science and engineering data embedded) will be re-formatted and assembled by JPL, generating the so-called Experiment Data Records (EDR). From REMS perspective, these EDR are low level instrument science and engineering data (raw voltages, counts, ...) at full resolution and time ordered. JPL is responsible for delivering these EDR assembled volumes to PDS according to the schedule stated by the mission.

Further processing levels, the so-called Reduced Data Records (RDR), are generated by the REMS team as part of the downlink data flow: in a first processing stage, electrical values and temperatures are estimated in combination with calibration information (these datasets are called TELRDR in REMS terminology); as a second processing step, environmental physical magnitudes are estimated (ENVRDR datasets); and finally, some corrections and models are applied in order to eliminate the rover's influence as well as other factors that may be altering the measurements (MODRDR datasets).

REMS team and the Centro de Astrobiología are responsible for generating and validating these RDR, and delivering those to PDS six months after landing, and in following intervals of three months along the mission life.

6 Summary

The REMS instrument onboard MSL has sensors that will record air and ground temperature, pressure, relative humidity, wind speed in the horizontal and vertical directions, as well as ultraviolet radiation in Mars. In this paper we describe the scientific potential of the measurements to be performed by REMS and its sensors.

Acknowledgements The authors thank José Barrera and all the great professionals from EADS-CRISA, which have participated in the project. We also wish to thank Jon Merrison from Aarhus University, for his collaboration on the wind tunnel tests with the wind sensor breadboards, as well as the team from Oxford University who also participated in the initial testing. Finally our thanks to the two reviewers of this paper and Ashwin Vasavada for their comments, which greatly helped to improve it.

The authors thanks to the Centro de Desarrollo Tecnológico e Industrial (CDTI), Ministerio de Economía y Competitividad (ESP2006-27267, ESP2007-65862, AYA2011-25720) and Instituto Nacional de Técnica Aeroespacial (INTA) of Spain for funding the project.

References

G. Amaral, J. Martínez-Frías, L. Vázquez, World Appl. Sci. J. **2**, 112–116 (2007)
C.A. Barth, C.W. Hord, Science **173**, 197–201 (1971)
C.A. Barth, C.W. Hord, A.I. Stewart, A.L. Lane, M.L. Dick, G.P. Anderson, Science **179**, 795–796 (1973)
T. Chamberlain, H.L. Cole, R.G. Dutton, G.C. Greene, J.E. Tillman, Bull. Am. Metereol. Soc. **57**, 1094–1104 (1976)
C.S. Cockell, D.C. Catling, W.L. Davis, K. Snook, R.L. Kepner, P. Lee, C.P. McKay, Icarus **146**, 343–359 (2000)
C. Cordoba-Jabonero, L.M. Lara, A.M. Mancho, A. Marquez, R. Rodrigo, Planet. Space Sci. **51**, 399–410 (2003)
C. Cordoba-Jabonero, M.-P. Zorzano, F. Selsis, M.R. Patel, C.S. Cockell, Icarus **175**, 360–371 (2005)
L.P. Daniel, NASA technical memorandum 102578 (1990)
M. Domínguez, V. Jimenez, J. Ricart, L. Kowakski, J. Torres, S. Navarro, J. Romeral, L. Castañer, Planet. Space Sci. **56**, 1169–1179 (2008)
F. Ferri, P.H. Smith, M. Lemmon, N. Renno, J. Geophys. Res. **108**, 5133 (2003)
J.A. Fisher, M.I. Richardson, C.E. Newman, M.A. Szwast, C. Graf, S. Basu, S.P. Ewald, A.D. Toigo, R.J. Wilson, J. Geophys. Res. **110**, E03004 (2005)
F. Forget, F. Hourdin, R. Fournier, C. Hourdin, O. Talagrand, M. Collins, S.R. Lewis, P.L. Read, J.-P. Huot, J. Geophys. Res. **104**, 24155–24176 (1999)
R. Greeley, D.A. Waller, N.A. Cabrol, G.A. Landis, M.T. Lemmon, L.D.V. Neakrase, M. Pendleton Hoffer, S.D. Thompson, P.L. Whelley, J. Geophys. Res. **115**, E00F02 (2010)
F. Gómez, E. Mateo-Martí, O. Prieto-Ballesteros, J. Martín-Gago, R. Amils, Icarus **209**, 482–487 (2010)
R.M. Haberle, H. Houben, R. Hertenstein, T. Herdtle, J. Atmos. Sci. **50**, 1544–1559 (1993a)
R.M. Haberle, J.B. Pollack, J.R. Barnes, R.W. Zurek, C.B. Leovy, J.R. Murphy, H. Lee, J. Schaeffer, J. Geophys. Res. **98**, 3093–3123 (1993b)
R.M. Haberle, M. Kahre, Mars **4**, 68–75 (2010)
A.-M. Harri, B. Fagerström, A. Lehto, G. Leppelmeier, T. Mäkinen, R. Pirjola, T. Siikonen, T. Siili, Planet. Space Sci. **46**, 1383–1392 (1998a)
A.-M. Harri, V. Linkin, J. Polkko, M. Marov, J.-P. Pommereau, A. Lipatov, T. Siili, K. Manuilov, V. Lebedev, A. Lehto, R. Pellinen, R. Pirjola, T. Carpentier, C. Malique, V. Makarov, L. Khloustova, L. Esposito, J. Maki, G. Lawrence, V. Lystev, Planet. Space Sci. **46**, 779–793 (1998b)
A.-M. Harri, T. Mäkinen, A. Lehto, H. Kahanpää, T. Siili, Planet. Space Sci. **54**, 1117–1123 (2006)
D.P. Hinson, M. Pätzold, S. Tellmann, B. Häusler, G.L. Tyler, Icarus **198**, 57–66 (2008)
C. Holstein-Rathlou et al., J. Geophys. Res. **115**, E00E18 (2010)
B.M. Jakosky, A.P. Zent, R.W. Zurek, Icarus **130**, 87–95 (1997)
B.M. Jakosky, R.M. Haberle, R.E. Arvidson, Science **310**, 1439–1440 (2005)
P.B. James, R.T. Clancy, S.W. Lee, L.J. Martin, R.B. Singer, E. Smith, R.A. Kahnand, R.W. Zurek, Icarus **109**, 79–101 (1994)
H. Kieffer, G. Neugebauer, G. Munch, J.R. Chase, E. Miner, Icarus **16**, 47–56 (1972)
A. Kliore, D.L. Cain, G.S. Levy, R. von Eshlema, G. Fjeldbo, D.F. Drake, Science **149**, 1243–1248 (1965)

S.E. Larsen, H.E. Jørgensen, L. Landberg, J.E. Tillman, Bound.-Layer Meteorol. **105**, 451–470 (2002)
M.C. Malin, M.A. Caplinger, S.D. Davis, Science **294**, 2146–2148 (2001)
M.P. Martín-Redondo, S. Martínez, M.T. Fernández Sampedro, C. Armiens, J. Gómez-Elvira, J. Martinez-Frias, J. Environ. Monit. **11**, 1428–1432 (2009)
D.J. McCleese, N.G. Heavens, J.T. Schofield, W.A. Abdou, J.L. Bandfield, S.B. Calcutt, P.G.J. Irwin, D.M. Kass, A. Kleinböhl, S.R. Lewis, D.A. Paige, P.L. Read, M.I. Richardson, J.H. Shirley, F.W. Taylor, N. Teanby, R.W. Zurek, J. Geophys. Res. **115**, E12016 (2010)
V.I. Moroz, E.V. Petrova, L.V. Ksanfomality, Planet. Space Sci. **41**, 569–585 (1993)
D.W. Mueller Jr., H.I. Abu-Mulaweh, Appl. Therm. Eng. **26**, 1662–1668 (2006)
L.M. Mukhin, A.P. Koscheev, Y.P. Dikov, J. Hurth, H. Ranke, Nature **379**, 141 (1996)
M.R. Patel, J.C. Zarnecki, D.C. Catling, Planet. Space Sci. **50**, 915–927 (2002)
M.R. Patel, A. Bérces, C. Kolb, P. Rettberg, J.C. Zarnecki, F. Selsis, Int. J. Astrobiol. **2**, 21–34 (2003)
M.R. Patel, A. Bärces, T. Kerekgyarto, G. Ronto, H. Lammer, J.C. Zarnecki, Adv. Space Res. **33**, 1247–1252 (2004a)
M.R. Patel, A.A. Christou, C.S. Cockell, T.J. Ringrose, J.C. Zarnecki, Icarus **168**, 93–115 (2004b)
S. Perrier, J.L. Bertaux, F. Lefevre, S. Lebonnois, O. Korablev, A. Fedorova, F. Montmessin, J. Geophys. Res. **111**, E09S06 (2006)
A. Petrosyan, B. Galperin, S.E. Larsen, S. Lewis, A. Maattanen, N. Renno, P. Rogberg, H. Savijärvi, T. Siili, A. Spiga, A. Toigo, L. Vazquez, Rev. Geophys. **49**, RG3005 (2011)
R.C. Quin, A.P. Zent, C.P. McKay, in *Lunar Planet. Sci. Conf. XXXII*, Houston, Texas, Boston (2001)
S.C. Rafkin, R.M. Haberle, T.I. Michaels, Icarus **151**, 228–256 (2001)
M. Ramos, M.A. de Pablo, E. Sebastián, C. Armiens, J. Gómez-Elvira, Cold Reg. Sci. Technol. **72**, 23–32 (2012)
M.I. Richardson, A.D. Toigo, C.E. Newman, J. Geophys. Res. **112**, E09001 (2007)
N.O. Renno, A.A. Nash, J. Lunine, J. Murphy, J. Geophys. Res. **105**(E1), 1859–1865 (2000)
R. Rodrigo, E. García-Alvarez, M.J. López-Gonzalez, J. Lopez-Moreno, J. Geophys. Res. **95**, 14795–14810 (1990)
E. Sebastián, C. Armiens, J. Gómez-Elvira, Appl. Therm. Eng. **30**, 2403–2411 (2010)
E. Sebastián, C. Armiens, J. Gómez-Elvira, Infrared Phys. Technol. **54**, 75–83 (2011)
A. Seiff, J. Tilman, J.R. Murphy, J.T. Schofield, D. Crisp, J.R. Barnes, C. LaBaw, C. Mahoney, J.D. Mihalov, G.R. Wilson, R. Haberle, J. Geophys. Res. **102**, 4045–4056 (1997)
M.D. Smith, M.J. Wolff, N. Spanovich, A. Ghosh, D. Banfield, P.R. Christensen, G.A. Landis, S.W. Squyres, J. Geophys. Res. **111**, E12S13 (2006)
M.D. Smith, Annu. Rev. Earth Planet. Sci. **36**, 191–219 (2008)
R. Sullivan, D. Banfield, J.F. Bell III, W. Calvin, D. Fike, M. Golombek, R. Greeley, J. Grotzinger, K. Herkenhoff, D. Jerolmack, M. Malin, D. Ming, L.A. Soderblom, S.W. Squyres, S. Thompson, W.A. Watters, C.M. Weitz, A. Yen, Nature **436**, 58–61 (2005)
P.A. Taylor, D.C. Catling, M. Daly, C.S. Dickinson, H.P. Gunnlaugsson, A.-M. Harri, C.F. Lange, J. Geophys. Res. **113**, E00A10 (2008)
P.A. Taylor, H. Kahanpää, W. Weng, A. Akingunola, C. Cook, M. Daly, C. Dickinson, A. Harri, D. Hill, V. Hipkin, J. Polkko, J. Whiteway, J. Geophys. Res. **115**, E00E15 (2010)
J.E. Tillman, N.C. Johnson, P. Guttorp, D.B. Percival, J. Geophys. Res. **98**(E6), 10,963–10,971 (1993)
J.E. Tillman, L. Landberg, S.E. Larsen, J. Atmos. Sci. **51**, 1709–1727 (1994)
L. Vázquez, M.-P. Zorzano, S. Jimenez, Opt. Lett. **32**, 2596–2598 (2007)
M.J. Wolff, R.T. Clancy, J.D. Goguen, M.C. Malin, B.A. Cantor, Icarus **208**, 143–155 (2010)
A.S. Yen, S.S. Kim, M.H. Hecht, M.S. Frant, B. Murray, Science **289**, 1909–1912 (2000)
M.-P. Zorzano, C. Córdoba-Jabonero, Icarus **190**, 492–503 (2007)
M.-P. Zorzano, L. Vázquez, S. Jimenez, Inverse Probl. **25**, 115023–115032 (2009)
M.-P. Zorzano, J. Martín-Soler, J. Gómez-Elvira, in *UV Photodiodes Response to Non-normal, Non-colimated and Diffusive Sources of Irradiance*, ed. by J.-W. Shi, Photodiodes—Communications, Bio-Sensings, Measurements and High-Energy Physics (InTech Publishers, Shanghai, 2011). ISBN:978-953-307-277-7